Electron tomography and optical modelling for organic solar cells

Viktor Andersson

Biomolecular and organic electronics
IFM
Linköpings universitet
Linköping, Sweden

Till Alexandra

Abstract

Organic solar cells using carbon based materials have the potential to deliver cheap solar electricity. The aim is to be able to produce solar cells with common printing techniques on flexible substrates, and as organic materials can be made soluble in various solvents, they are well adapted to such techniques. There is a large variation of organic materials produced for solar cells, both small molecules and polymers. Alterations of the molecular structure induce changes of the electrical and optical properties, such as band gap, mobility and light absorption. During the development of organic solar cells, the step of mixing of an electron donor and an electron acceptor caused a leap in power conversion efficiency improvement, due to an enhanced exciton dissociation rate. Top performing organic solar cells now exhibit a power conversion efficiency of over 10%. Currently, a mix of a conjugated polymer, or smaller molecule, and a fullerene derivative are commonly used as electron donor and acceptor. Here, the blend morphology plays an important role. Excitons formed in either of the donor or acceptor phase need to diffuse to the vicinity of the donor-acceptor interface to efficiently dissociate. Exciton diffusion lengths in organic materials are usually in the order of 5-10 nm, so the phases should not be much larger than this, for good exciton quenching. These charges must also be extracted, which implies that a network connected to the electrodes is needed. Consequently, a balance of these demands is important for the production of efficient organic solar cells.

Morphology has been found to have a significant impact on the solar cell behaviour and has thus been widely studied. The aim of this work has been to visualize the morphology of active layers of organic solar cells in three dimensions by the use of electron tomography. The technique has been applied to materials consisting of conjugated polymers blended with fullerene derivatives. Though the contrast in these blends is poor, three-dimensional reconstructions have been produced, showing the phase formation in three dimensions at the scale of a few nanometres. Several material systems have been investigated and preparation techniques compared.

Even if excitons are readily dissociated and paths for charge extraction exist, the low charge mobilities of many materials put a limit on film thickness. Although more light could be absorbed by increased film thickness, performance is hampered due to increased charge recombination. A large amount of light is thus reflected and not used for energy conversion. Much work has been put into increasing the light absorption without hampering the solar cell performance. Aside from improved material properties, various light trapping techniques have been studied. The aim is here to increase the optical path length in the active layer, and in this way improve the absorption without enhanced extinction coefficient.

At much larger dimensions, light trapping in solar cells with folded configuration has been studied by the use of optical modelling. An advantage of these V-cells is that two materials with complementing optical properties may be used together to form a tandem solar cell, which may be connected in either serial or parallel configuration, with maintained light trapping feature. In this work optical absorption in V-cells has been modelled and compared to that of planar ones.

Populärvetenskaplig sammanfattning

Organiska solceller kan erbjuda ett billigt sätt att konvertera solljus till elektrisk energi. I denna typ av solceller används plastmaterial, lösliga i organiska lösningsmedel, för att åstadkomma detta. Fördelen med dessa material är att de kan appliceras med trycktekniska metoder, vilket innebär lägre produktionskostnader, jämfört med konventionella solceller. Även om material och tillverkningsmetoder ständigt utvecklas, med högre verkningsgrader som följd, är det önskvärt att höja prestandan och bättre förstå vad som påverkar denna, för att kunna ta fram effektivare och mer hållbara material och solceller.

I sin enklaste form består en solcell av ett aktivt lager, där energikonverteringen sker, placerad mellan två elektroder. I de organiska solceller som studerats i detta arbete är det aktiva lagret en ca 100 nm tjock halvledare, där en polymer och en mindre molekyl, vilka fungerar som elektrondonator och -acceptor, är blandade. När ljus absorberas av endera materialet flyttas elektroner till ledningsbandet och lämnar kvar hål i valensbandet. Dessa par av negativt laddade elektroner och positivt laddade hål bildar excitoner som måste separeras för att ström ska kunna extraheras ur solcellen. I de organiska solcellerna krävs det dock relativt mycket energi för att göra detta. Därav materialblandningen. Elektrondonatorns och -acceptorns energinivåer skiljer sig från varandra, vilket innebär att det är energimässigt fördelaktigt för elektronerna att överföras till acceptorns ledningsband. Detta betyder att hål och elektroner lättare kan separeras och bidra till strömmen. Denna överföring sker i gränsytorna mellan materialen, och materialfördelningen är därför viktig för solcellsfunktionen. Eftersom excitonerna måste hinna diffundera till en gränsyta innan hål och elektroner rekombinerar krävs tillräckligt små materialdomäner för att generera höga strömmar. Samtidigt ska de genererade laddningarna transporteras till elektroderna, utan att hål och elektroner rekombinerar, varför det krävs ett nätverk av transportvägar. En kombination av dessa kriterier

är alltså nödvändigt för effektiva celler, och därför kan samma material i olika morfologier ge olika prestanda. Lösningsmedel, koncentration, material, och beläggningsmetod kan alla påverka det aktiva lagrets slutliga utseende och eftersom morfologin är viktig har mycket arbete lagts på, och många tekniker använts för, att undersöka denna.

I detta arbete har elektrontomografi använts för att undersöka det aktiva lagrets morfologi. I denna teknik används ett transmissionselektronmikroskop (TEM) för att samla in data, vilka består av projektioner ur flera vinklar av det aktiva lagret. De genererade bilderna används sedan för att göra en tredimensionell rekonstruktion. TEM ger möjlighet till några nanometers upplösning, och trots att både donator och acceptor till största delen består av kol är kontrasten tillräcklig för att möjliggöra rekonstruktioner.

Här har elektrontomografi använts till att jämföra material och tillverkningsvillkor. Metoden har varit speciellt användbar för att jämföra material liknande varandra, där exempelvis olika lösningsmedel använts. Till synes små förändringar i processvillkoren har visat sig kunna ge stora skillnader i materialens utseende. Några generella slutsatser gällande sambandet mellan morfologi och prestanda har dock varit svårt att dra, vilket pekar på komplexiteten hos laddningsgenereringen i organiska solceller.

Då laddningarnas rörlighet ofta är låg i materialen används tunna filmer för att lättare extrahera laddningarna. Nackdelen med tunna filmer är att mycket ljus reflekteras bort, och därför är ljusinfångning, där ljuset leds en längre väg genom det aktiva lagret, av intresse. Här kan mer ljus absorberas utan att laddningarna får svårare att nå elektroderna.

En enkel metod för att fånga ljus är att använda en vikt, V-formad, solcell, som här har studerats med hjälp av optisk modellering. Den V-formade strukturen ger upphov till multipla reflektioner mellan V:ets ben, och därmed en ökad absorption. Dessutom kan olika material, med skilda absorptionsspektra, placeras på de två sidorna för att på det sättet bilda en tandemcell. Absorptionen i dessa vikta strukturer har beräknats och jämförts med plana solceller.

List of publications

Publications included in thesis

Paper 1
Imaging of the 3D Nanostructure of a Polymer Solar Cell by Electron Tomography
B. Viktor Andersson, Anna Herland, Sergej Masich, and Olle Inganäs
Nano Letters 9, 953 (2009)

Paper 2
Nanomorphology of Bulk Heterojunction Organic Solar Cells in 2D and 3D Correlated to Photovoltaic Performance
Sophie Barrau, Viktor Andersson, Fengling Zhang, Sergej Masich, Johan Bijleveld, Mats R. Andersson, and Olle Inganäs.
Macromolecules 42, 4646 (2009)

Paper 3
The Effect of additive on performance and shelf-stability of HSX-1/PCBM photovoltaic devices
Weiwei Li, Yi Zhou, B. Viktor Andersson, L. Mattias Andersson, Yi Thomann, Clemens Veit, Kristofer Tvingstedt, Ruiping Qin, Zhishan Bo, Olle Inganäs, Uli Würfel, and Fengling Zhang.
Organic Electronics 12, 1544 (2011)

Paper 4
Lateral Phase Separation Gradients in Spin-Coated Thin Films of High-Performance Polymer:Fullerene Photovoltaic Blends
Lintao Hou, Ergang Wang, Jonas Bergqvist, B. Viktor Andersson, Zhongqiang Wang, Christian Müller, Mariano Campoy-Quiles, Mats R. Andersson, Fengling Zhang, and Olle Inganäs.
Advanced Functional Materials 21, 3169 (2011)

Paper 5
Morphology of organic electronic materials imaged via electron tomography
B.Viktor Andersson, Sergej Masich, Niclas Solin, and Olle Inganäs.
In manuscript

Paper 6
Optical modeling of a folded organic solar cell
Viktor Andersson, Kristofer Tvingstedt, and Olle Inganäs.
Journal of Applied Physics 103, 094520 (2008)

Paper 7
Comparative study of organic thin film tandem solar cells in alternative geometries
B. Viktor Andersson, Nils-Krister Persson, and Olle Inganäs.
Journal of Applied Physics 104, 124508 (2008)

Paper 8
Full day modelling of V-shaped organic solar cell
B. Viktor Andersson, Uli Wuerfel, and Olle Inganäs.
Solar Energy 85, 1257 (2011)

Paper 9
An optical spacer is no panacea for light collection in organic solar cells
B. Viktor Andersson, David M. Huang, Adam J. Moulé, and Olle Inganäs.
Applied Physics Letters 94, 043302 (2009)

Author's contribution

Paper 1
Part of electron tomography measurements. Main part of the writing.

Paper 2
Electron tomography measurements. Contribution to the writing.

Paper 3
Electron tomography measurements and contribution to the writing.

Paper 4
Electron tomography measurements and optical modelling of devices. Con-

tribution to the writing.

Paper 5
Measurements and main part of the writing.

Paper 6
Optical modelling and main part of the writing.

Paper 7
Optical modelling of the V-shaped structure and main part of the writing.

Paper 8
Optical modelling of devices. Main part of the writing.

Paper 9
Optical modelling of devices with APFO-3:PCBM and APFO-Green5:PCBM, and preparation of data and figures.

Publication not included in thesis

Folded reflective tandem polymer solar cell doubles efficiency
Kristofer Tvingstedt, Viktor Andersson, and Olle Inganäs.
Applied Physics Letters 91, 123514 (2007)

Acknowledgements

I would like to thank all people who have helped me during my time at IFM and supported me in the life outside. Some help and suggestions have been directly applicable, while other have been useful in the thought-process along the research road.

Firstly, I would like to thank Olle Inganäs, who introduced me to the field of organic electronics, employed me, and have supervised me during these years. To me, our discussions have been stimulating and encouraging, and have helped me see problems from another angle.

A big thank you goes to Sergej Masich, who has been a great help with the practicalities of electron tomography, both hardware and software, as well as discussions concerning reconstructions and interpretation. Not to mention those valuable lunch breaks.

Here, I also want to thank Anna Herland, who began the tomography studies in the group and helped me a lot in the start-up process.

Nils-Krister Persson has been very helpful in the joint work with optical modelling. I appreciate both discussions and data and wish for success in future rodent fights.

I want to thank Kristofer Tvingstedt, who guided me into the land of polymers and reflections and have always been generous with knowledge and suggestions, for collaboration and solar cell conversations. I have found the discussions, questions and answers very helpful.

Solvents, iron distributions, and other chemistry related questions have been enlightened with the help of Niclas Solin, to whom I am thankful. I do not yet fully comprehend the historical logics of Japanese sign construction, though.

I thank Fengling Zhang for all practical help, sample supply and discussions. To Sophie Barrau, David Huang, Adam Moulé, Lintao Hou, Weiwei Li, Uli Würfel, Per Persson, Jonas Bergqvist, Christian Müller, Anders Elfwing, Jens Wigenius and Koen Vandewal I am grateful for data, materials, help, discussions and ideas. All members of the Biorgel group and their combined diverse knowledge have been inspiring during the years. Bo

Contents

1

Introduction

The use of organic solar cells (OSCs) [1–3] may be a potential route for filling the increasing need of energy by the exploitation of the long lived sun. Organic materials, such as polymers, may be used for the deposition of films on plastic substrates by common printing methods. The aim is to keep the material and production costs down, while maintaining a high production rate. Thus, the price of extracted energy is kept low, which is vital if the technology is to be able to compete with its inorganic cousins. Although progress in improving material and devices has been seen the recent years, with PCEs over 8%, [4] more may still be done. Often, a 10% power conversion efficiency (PCE) is claimed to be needed for commercialisation of OSCs, and a PCE of 10% was recently reported. [5] Along with the need of cheap and efficient solar cells is the need for stability. It is common that OSCs suffers from short life times. [6] Water and oxygen can have a severe effect on the layers and layer interfaces comprising the solar cell, and cause degradation. Reorganisation of the active layer may also be a cause of decreased performance. Good, but still cheap, encapsulation may be a solution to this problem.

As part of the strive towards more efficients OSCs is the synthesis of new materials, [7] with better light absorption, higher charge mobilities and better mechanical properties. As the active layer, where the energy conversion takes form, of OSCs is often consisting of a blend of an electron donor and an electron acceptor, the miscibility of these and their solubility in miscellaneous solvents are among the important properties.

Over the years, solar cells prepared with the use of different materials or solvents and posttreated in various ways have been thoroughly studied. As the morphology is of large importance for the behaviour of OSCs it has been examined in many ways, and is also a large part of this thesis. Many techniques (see 2.1) can be used to image the surface of e.g. polymer

layers, or extract information such as crystal sizes or stoichiometry from the bulk, but since light is absorbed in all of the active layer the possibility to image the layer in three dimensions, with good resolution, is of importance. However, it is only recently that the technique of electron tomography has been applied to OSCs.

1.1 Polymers

The function of any photovoltaic cell (see 1.2) is based on the use of semi-conducting materials in the active layer. In the devices studied here, semi-conducting polymers and fullerene derivatives have been used.

Polymers are molecules consisting of several identical units called mers, hence the name. Carbon is commonly the main constituent here, and the mers are covalently bonded. In a polymer the number of mers are sufficient to leave some material properties, e.g. melting temperature, unaltered by the addition or removal of a mer. The number of building blocks needed may of course differ for different properties, which means that the material may be a polymer in some sense, but not in others. A common, and simple, polymer is polyethylen (or polythene) (PE) shown in figure 1.1. The name comes from the starting material, ethene, in the polymerization process. In figure 1.1 the PE molecule is seen as a long chain of covalently bonded
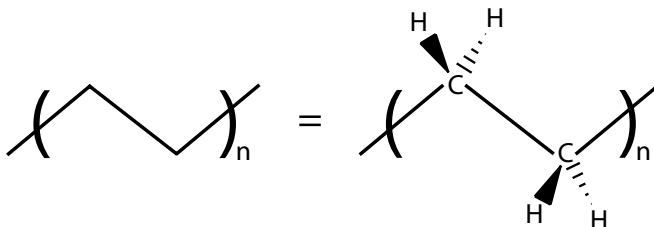
Figure 1.1: Molecular structure of polyethylene. The polymer consist of n mers.

carbon atoms, with hydrogen atoms attached. The covalent bonds in the molecule is the overlap of atomic orbitals (AOs), forming molecular orbitals (MOs). In carbon the s- and p-orbitals can be seen to be combined into hybrid orbitals, called sp^3-, sp^2- and sp-orbitals, depending on the ratio of s and p character. The reason for this hybridisation is a reduction in energy and better overlap of the atomic orbitals, [8]. In figure 1.2 probability iso-surfaces of the orbitals are schematically depicted. The actual shape of the orbitals are somewhat different, but they are here sketched to emphasise the
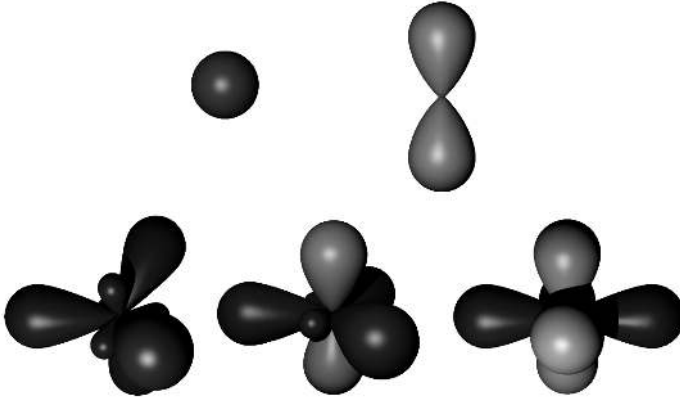
Figure 1.2: Schematic pictures of atomic and hybrid orbitals. From top left to bottom right: s-, p-, sp^3-, sp^2-, and sp-orbitals.

important directional characteristics. In PE carbon molecules are bonded to two other carbons, by overlap of the sp^3-orbitals, and to two hydrogens, by overlap of the carbon sp^3-orbitals and hydrogen s-orbitals, named σ-bonds. In a conjugated polymer, e.g. polyacetylen (or polyethyne) (PA) (see figure 1.3) C-C and C-H bonds is formed in the same way. However, here the AOs in carbon is sp^2-hybridized, with two of the sp^2-orbitals overlapping sp^2-orbitals of adjacent carbons and one overlapping the s-orbital of a hydrogen. The remaining p-orbital (light grey in figure 1.2) form, together with one at the adjacent carbon, the other part of the double bond, named π-bond.

Figure 1.3: Molecular structure of the conjugated polymer polyacetylene.

The linear combinations of orbitals into molecular orbitals comes together with the formation of band structures, relating the orbital energy and the wave vector, k, of the wave function of the MO. In conjugated polymers alternating double and single bonds are found. These are associated with differences in bond lengths and a reduction in energy, compared

to the case with equal bond lengths.

The existence of π-bonds and orbitals gives the conjugated polymers semiconducting properties, with band gaps depending on the structure of the molecule. This, together with decent hole mobilities, makes them suitable as solar cell materials.

The conductivity is, however, poor in a neat conjugated polymer. If the material is doped, by oxidation or reduction, the conductivity may increase dramatically as charges are made free to move. As an example, Poly(3,4-ethylenedioxythiophene):poly(styrenesulfonate) (PEDOT:PSS), which is widely used as anode in OSCs, may be mentioned. The molecular structure of PEDOT:PSS is seen in figure 1.4. Some of the sulfonyl groups are deprotonated and negatively charged, while PEDOT is positively charged.
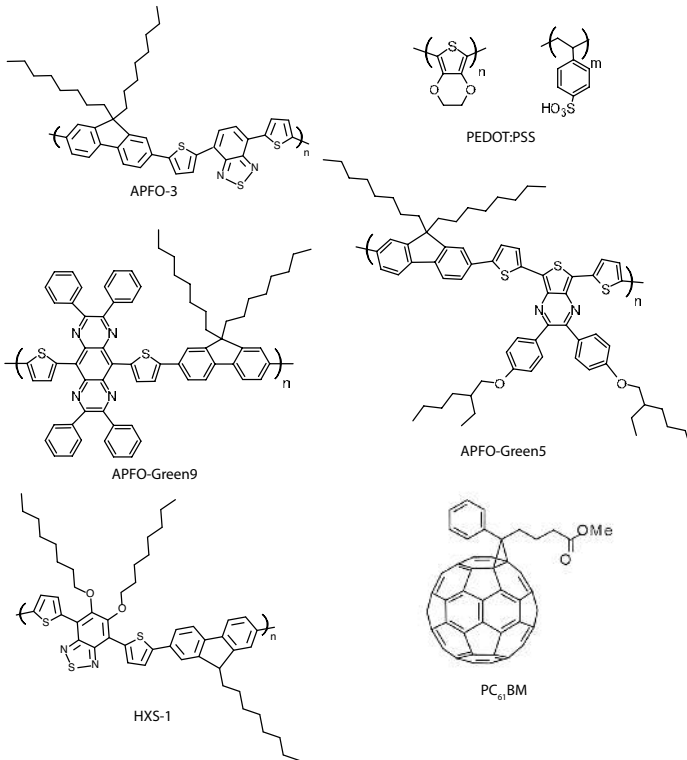

Figure 1.4: Examples of organic electronic materials used in solar cells.

As polymers or polymers and smaller molecules are mixed in a cooling melt or drying solution, phase separation may occur, depending on the

interaction between molecules, both of the same and the other species. [9–11] This has a large influence on the morphology of the active layer of OSCs, as these are made of a blend between an electron donating and an electron accepting material. Often the donor is a conjugated polymer and the acceptor a fullerene derivative, e.g. $PC_{61}BM$ or $PC_{71}BM$. Examples of polymers used in the active layer of solar cells is found in figure 1.4, together with the fullerene derivative $PC_{61}BM$.
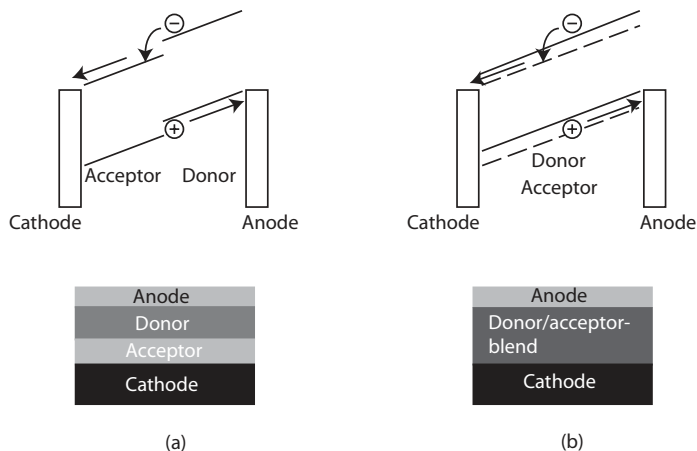
1.2   Organic solar cells

In a solar, or photovoltaic, cell light is converted to electrical energy. The basic construction of a solar cell is a semiconducting material between two electrodes with differing work functions. As light is absorbed the semiconductor is excited, whereby an electron is moved to a higher energy level in the conduction band, and leaves a hole in the valence band. During operation, a voltage is applied over the cell, which affects the electric field within the semiconductor. (See fig 1.5) If the applied voltage is less than the open circuit voltage, e.g. at short circuit, a gradient in the energy levels will be present, since the anode and cathode have different work functions, which will drive the charges towards the electrodes. In figure 1.5 the highest occupied MO (HOMO) and lowest unoccupied MO (LUMO), i.e. the edge of the valence band and conduction band, respectively, are schematically described. The short circuit and open circuit case, i.e. anode and cathode are connected or disconnected, are illustrated.
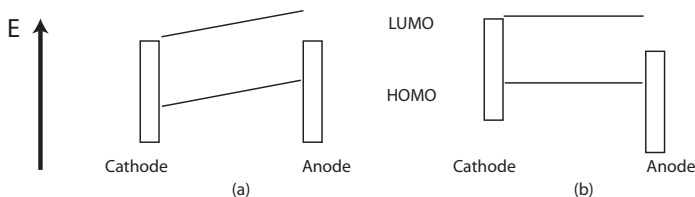
Figure 1.5: Energy levels in solar cells at (a) short circuit and (b) open circuit.

To extract an electrical current from the device, some difficulties need to be handled. The efficiency with which the solar cell device transform energy, η, is limited by all steps from light absorption to charge extraction, and can be compactly written

$$\eta = \eta_{abs} \cdot \eta_{diff} \cdot \eta_{dis} \cdot \eta_{trans} \cdot \eta_{col} \tag{1.1}$$

Figure 1.6: Schematic picture of energy conversion in organic solar cells. (a) shows a bilayer cell (bottom) and corresponding energy levels (top). (b) shows a bulk heterojunction cell (bottom) and corresponding energy levels (top).

where all included efficiencies could be wavelength or electric field dependent. First, the active layer needs to absorb the incoming light efficiently, which may be achieved by using materials with large absorption coefficients, thick layers or light trapping configurations. [12–18] This efficiency is described by η_{abs}, which includes losses by reflection and parasitic absorption in other layers, such as electrodes. Commonly, the active layer of an OSC is around 100 nm thick, which is rather thin for efficient light absorption. The reason for not using thicker layers, which would result in sufficient light absorption without the need for light trapping features, is that the electrical properties of the solar cell is hampered. The charge mobilities of the organic materials used are usually too small to allow for thick active layers.

When the organic semiconductor is excited, free charges are not immediately produced. Instead excitons are formed, which are coulombically bound electron-hole pairs. In inorganic materials, such as Si, the exciton binding energies are small, [19] due to a higher dielectric constant, screening the charges. The excitons can therefore separate into free charges, with small Coulomb interaction, thermally. However, in organic materials, such as conjugated polymers, the exciton binding energies can be as large as 1 eV [20], far larger than $k_B T$. Thus the exciton is unlikely dissociated into free charges in the neat polymer, but will recombine, resulting in a small current. An effective solution to this problem is to use two materials, of

which one is an electron donor and one an electron acceptor, to form the active layer. The materials should be designed such that the LUMO and HOMO of the donor exhibits a higher energy than the LUMO and HOMO of the acceptor. Such cells are schematised in figure 1.6, both in bilayer and bulk heterojunction configuration. After excitation the excitons are diffusing around and may, with probability η_{diff}, encounter an acceptor-donor interface before they recombine. An electron of such an exciton, in the donor phase, situated at the interface between the donor and acceptor will, due to the electron affinity difference, be driven to the LUMO of the acceptor. At this stage there may still be a coulombic electron-hole interaction, small enough for the charges to overcome with the help of the electro-chemical potential difference. The dissociation of excitons is achieved with efficiency η_{dis}, possibly via a charge transfer (CT) exciton, where the electron and hole are situated in the acceptor and donor phase, respectively

After dissociation the electron and hole are driven towards the contacts, where they are collected. The transport and collection efficiencies are described by η_{trans} and η_{col}, respectively. A good match between anode work function and donor HOMO, and between cathode work function and acceptor LUMO, results in a larger V_{oc} and inner electric field, and good extraction of current. [21]

Good extraction of free charge carriers (high η_{trans}) requires the existence of pathways, in each of the phases, from the dissociation site to the contacts, where charges are collected. Isolated islands of one phase in the other will result in trapped charges, eventually recombining. [22] Free pathways are self-evident when a bilayer configuration, where the donor is placed on top of the acceptor, is used. However, only the excitons generated within the diffusion length from the donor-acceptor interface can be dissociated and contribute to photocurrent. As the diffusion length is typically 5-10 nm [23–25] for conjugated polymers much light is lost in the bilayer configuration; thick layers, though effectively absorbing, will result in much energy dissipation far from the donor-acceptor interface, while layer thicknesses closer to the exciton diffusion length means higher η_{dis}, but less absorption. A successful architecture of the donor-acceptor solar cell is the bulk heterojunction, where the donor and acceptor are blended, forming an entangled network within the active layer. The mixing produces a much larger total interface area and smaller exciton to interface distances than in the bilayer cell. The existence of free pathways is, however, not as obvious here as in the bilayer case.

The macroscopic behaviour of solar cells is tested by current-voltage (JV) measurements, from which much information can be gained. Figure 1.7 displays an example of such a JV-curve. Important features are short circuit current density (J_{sc}), open circuit voltage (V_{oc}) and fillfactor (FF). Short

circuit current is the current gained without any applied field and open circuit voltage the voltage applied to produce no current. For high power conversion efficiency both high J_{sc} and V_{oc} is desired, together with a large FF. The FF is illustrated as a shaded box in figure 1.7 and is the ratio between the power extracted at the maximum power point (MPP) and the product of J_{sc} and V_{oc}, i.e. $f_{FF} = max(|J \cdot V|)/|J_{sc} \cdot V_{oc}|$. A small serial resistance (R_s) is desirable for easy charge extraction, while the parallel resistance (R_p) should be high, which corresponds to a small amount of shunts. A small R_s and large R_p improve the fill factor.
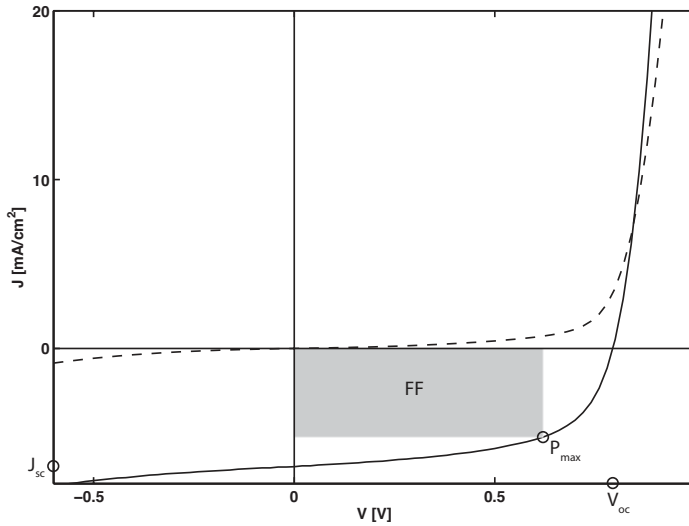
Figure 1.7: Example of JV-curve, under illumination (——) and in the dark (- - -). Short circuit current (J_{sc}), open circuit voltage (V_{oc}) and maximum power point (P_{max} are shown. The fill factor (FF) is indicated as the grey box.

Another useful measurement is the external quantum efficiency (EQE) which is the wavelength resolved ratio between the number of extracted electrons and the number of incident photons. The related internal quantum efficiency (IQE) is, although not directly measurable, also important, as it describes the ratio between the number of extracted electrons and the number of absorbed photons in the active layer.

The open circuit voltage is closely related to the band gap of the active material. [2,26] Since only photons with energy larger than the bandgap are absorbed, this means that there is a trade off between voltage and current. A smaller bandgap provides the possibility for more light to be absorbed

and contribute to current, but is at the same time lowering the voltage. For better use of photon energy, tandem cells may be utilised. [27] In these cells more than one active layer is used for energy conversion of different wavelength regions. By the smaller energy losses higher efficiencies can be reached. [28] The purpose of a tandem cell is to diminish the energy loss of absorbed photons by using several bandgaps, as illustrated in figure 1.8, and the principle is to direct different parts of the solar spectrum onto subcells with appropriate bandgaps. An easy way of directing is to use the subcells
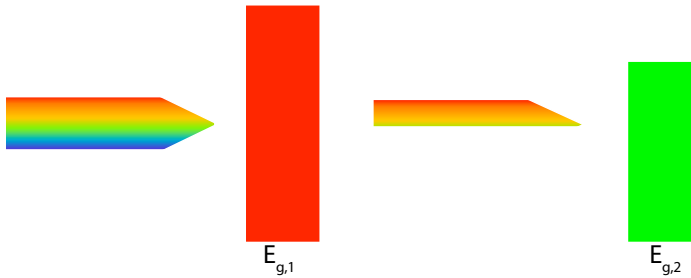
Figure 1.8: Principle of a stacked tandem solar cell. The light is energetically filtered while absorbed by the subcells.

themselves as filters. With several active layers a higher bandgap may be used to absorb the high-energy photons, resulting in a smaller loss of energy due to thermal relaxation.

1. _____

2

Morphology in blends and organic solar cells

The better mixed and homogeneous the blend of a bulk heterojunction solar cell is, the smaller the exciton diffusion length need to be, but the chance of finding isolated islands, not connected to the electrodes, will be larger. Moreover, smaller domains mean less charge delocalization, which may work against efficient charge separation. [29,30] The morphology of the active layer is thus of large importance in bulk heterojunction cells and a beneficial morphology shows both a large interface area and good connection between potential dissociation sites and the contacts together with domains large enough for efficient exciton dissociation. Donor polymers and acceptor molecules are commonly mixed in a common solvent, or solvent blend, for deposition on a substrate, where the morphology develops during solvent evaporation. Thus, the possibility to direct control of the morphology formation is minute. Changes in solvent, molecular structures, blend ratio, concentration and deposition technique are all variables affecting the final morphology.

Thus, phase formation in organic solar cells is of importance, both for energy conversion and charge extraction. The desired dimensions of the phases is dependent on mean exciton diffusion lengths, recombination rates and charge mobilities, which are all dependent on the materials involved.

Phase separation of polymer blends in general has been thoroughly studied and Flory-Huggins theory is often used to describe the behaviour of polymer blends. [9] It is the continuation of the theory of molecular solutions to blends comprising long molecules. From the assumption that each mer in a polymer occupies one virtual lattice point in a volume of mixture, the change of free energy upon mixing of two components, a and b, can be

described by

$$\frac{\Delta G}{k_B T} = \frac{\phi_a}{N_a} \ln \phi_a + \frac{1 - \phi_a}{N_b} \ln(1 - \phi_a) + \chi \phi_a (1 - \phi_a) \qquad (2.1)$$

where ΔG is the change in Gibb's free energy per site upon mixing, ϕ_a is the fraction of component a and $1 - \phi_a = \phi_b$ fraction of component b. N_a and N_b is the number of segments of species a and b, respectively. χ is the interaction parameter, describing the contact energy between segments [10]

$$\chi = \frac{2E_{ab} - E_{aa} - E_{bb}}{2k_B T} \qquad (2.2)$$

Here, E_{ij} represents the contact energy between components i and j, k_B is Boltzmann's constant and T the temperature. In the absence of interacting forces such as hydrogen bonds, the interaction energy between segments of the same species is smaller than between differing species, giving a positive parameter χ. Thus, the first two terms of eq. 2.1 describe the entropic part which acts to mix the two components, while the last term, describing the interaction energy that acts to separate the materials. In figure 2.1 is the interaction of all terms of the right hand side of eq. 2.1 exemplified. Four
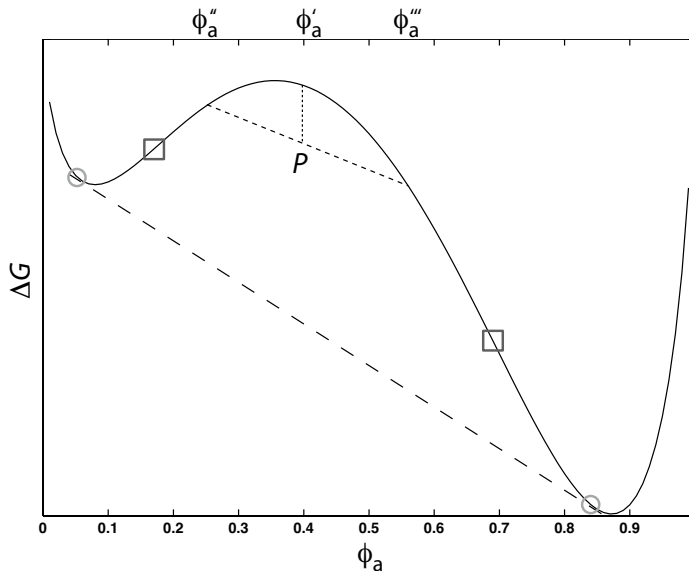
Figure 2.1: Free energy of mixing as function of concentration of component a. Spinodal (squares) and binodal (circles) points are marked.

points are marked in figure 2.1, namely the binodal and spinodal points. The spinodal points are the inflection points of ΔG. Between the spinodal points $\partial^2 \Delta G / \partial \phi_a^2 < 0$, meaning that the composition is unstable to any fluctuations in concentration. A phase with concentration ϕ_a' is associated with a higher energy than two phases with concentrations ϕ_a'' and ϕ_a''', as in figure 2.1. The volume of these phases are determined by

$$V'' \phi_a'' + V''' \phi_a''' = V_{tot} \phi_a' \tag{2.3}$$

and

$$V'' + V''' = V_{tot} \tag{2.4}$$

which describe mass and volume conservation, respectively. These equations give the free energy per segment corresponding to point P in figure 2.1. A blend with concentration ϕ_a' will thus phase separate, by spinodal decomposition, without experiencing any energy barrier.

The binodal points are distinguished by equilibrium conditions. That is that the chemical potential of the two components are equal in the two phases, and these points have a common tangent in the plot of ΔG.

Between the binodal and spinodal point the blend is metastable, meaning that small concentration fluctuations will increase the total free energy, while larger fluctuations will decrease the energy. In this region there is an energy barrier that needs to be overcome for phase separation to occur. This free energy barrier of nucleation that the system needs to overcome is larger further away from the spinodal point. Phase separation of a blend in the metastable region occurs by nucleation and growth, where small droplets of one material form and grow until equilibrium conditions are reached. [10] Once equilibrium is reached growth of phases proceeds by Ostwald ripening, where large particles grow at the expense of smaller ones. Figure 2.2 illustrates typical morphologies obtained by spinodal decomposition and nucleation in binary blends.

If the interaction parameter, χ, is changed, so is ΔG. Thus a phase diagram may be constructed, where the phase characteristics are plotted as function of concentration and interaction parmeter. An example is seen in figure 2.3. In the phase diagram the spinodal and binodal points are plotted, as these describe instability and equilibrium limits. The critical point is where the spinodal and binodal curves meet. Below this point the blend is easily mixed to one phase. Often the phase diagram is plotted as function of temperature, where the critical point is either an upper or lower critical solution temperature, depending on the temperature dependence of χ.

A common approach to film formation in OSCs is spin coating, where the blend solution is applied to the substrate, placed on a rotatable chuck. As the substrate is set to rotate the solution is spread out and dried, while the
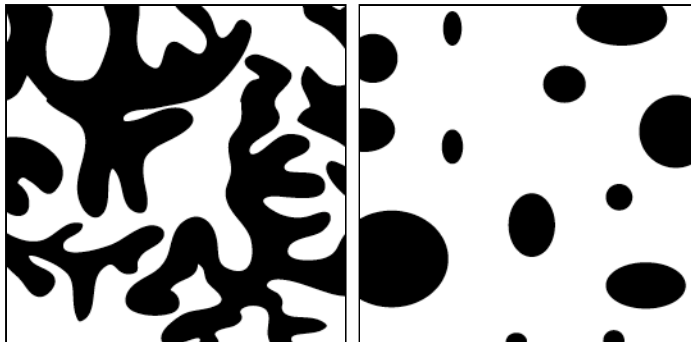
Figure 2.2: Illustration of morphologies in blends undergoing spinodal decomposition (left) and nucleation and growth (right).

film is formed. Here, the solubility of the two materials in the solvent blend, together with the concentration, spin speed and the evaporation rate governs the film formation. The films produced are usually thin, so the development of phases is confined between the substrate and air interfaces. [31]

In the case of spin coating the system goes from low concentration and a well mixed phase to a high concentration quickly as the solvent is evaporated. Therefore, there is seldom enough time for the system to reach equilibrium conditions. The system is said to be quenched in this process, and the final structure is difficult to foresee. A fast evaporting solvent freezes the materials quickly, by giving them little time to reorganise in accordance to material interaction energies. Thus films formed from such solvents may exhibit a far from equilibrium structure. The formation of $PC_{61}BM$-crystallites, due to limited solubility, in slow-drying polymer:$PC_{61}BM$ films has been observed. This led to a morphology of finely dispersed fullerene crystals, which can be compared to general case of blends, where slow drying means time for phase separation. [32]

The solvents used has proven to be of large importance for the film morphology, both in blends for OSCs and blends of insulating polymers. [33–42] The use of solvent blends, with one main solvent and an additional, less volatile, solvent has been successfully applied for morphology improvements in OSCs. [38–40]

Also important for formation of thin films by spin coating is the surface energy at the substrate and air interfaces. [42] A preferential wetting by one component can introduce a vertical concentration gradient, [43–46] even though the interface effect may be localised close to the surface. A homogenous mixture in a bulk sample, which is quenched into the spinodal re-
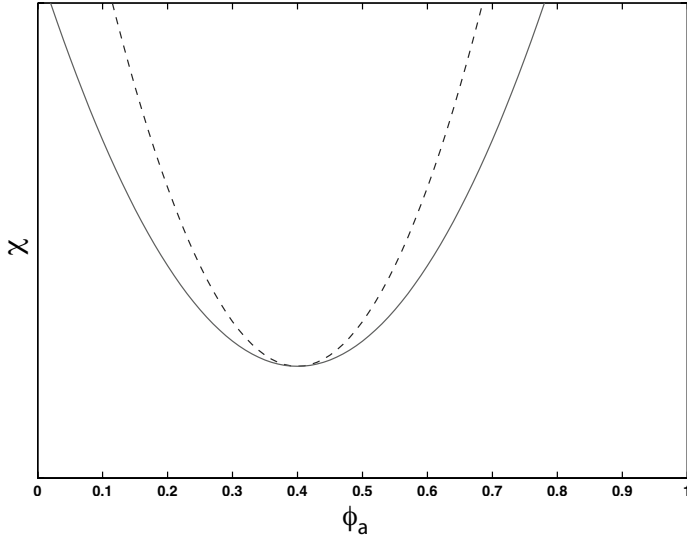
Figure 2.3: Schematic example of phase diagram, where spinodal (- - -) and binodal (—) points are shown as function of interaction parameter, χ.

gion undergo decomposition showing spinodal waves with some wavelength, random in phase, amplitude and direction. [47] In a thin film, surface effects may play a crucial roll, as the component with the smallest surface energy tend to segregate to the surface. This induces spinodal waves, and decomposition, directed orthogonal to the surface.

In addition to the fast quenching and surface energy, the confined geometry of the thin sample is also a factor in the formation of active layers via spin coating, where thicker layers allow for the growth of larger phases.

Posttreatment, e.g. thermal or vapour annealing, is common in fabrication of some organic solar cells. The mobility of the components can be improved by heating and the system can faster move towards thermal equilibrium. Postannealing is especially common for crystalizing materials, where the degree of crystalization may increase, with improved charge transport characteristics. [48–50] This is, however, not a general result. [51]

The influence of morphology on OSC characteristics is mainly seen as altered charge mobilities, light absorption, currents and fill factors, due to phase aggregation. [22,34,35,38,52–54] Crystallised materials often exhibit a smaller voltage due to the increased packing and lowered energy states. [54]

Morphology also plays a role for charge separation, where larger domains

often seem to facilitate exciton dissociation. This can be understood by considering the increased delocalization volume available in a coarse morphology compared to a finer one. [29, 30]After the diffusion of an exciton formed in either phase, a charge transfer exciton is formed. The charge transfer state is localised on both donor and acceptor and has a lower energy than the donor or acceptor exciton in a well performing solar cell. These excitons are not as tightly bound as the pure phase excitons and may be dissociated by the help af an applied electric field. The larger polaron pair radius, which accompanies more delocalized charges, decrease the coulombic force and makes the splitting easier. An increased, local, charge mobility, due to clustering may also be influential in the separation of charges. [29, 30]

The morphology can also be seen to change with the donor-acceptor ratio, [30,32,55–58] and the stoichiometry is thus of importance for the solar cell behaviour also in this sense, with larger fullerene domains in blends with high acceptor content. In addition to affecting exciton separation efficiency, charge transport properties are modulated. A larger amount of fullerenes produce a better connected network for extraction, as well as improving both hole and electron mobilities. [59, 60]

In figure 2.4 is an example of stoichiometry dependent morphology. Here,

100 nm
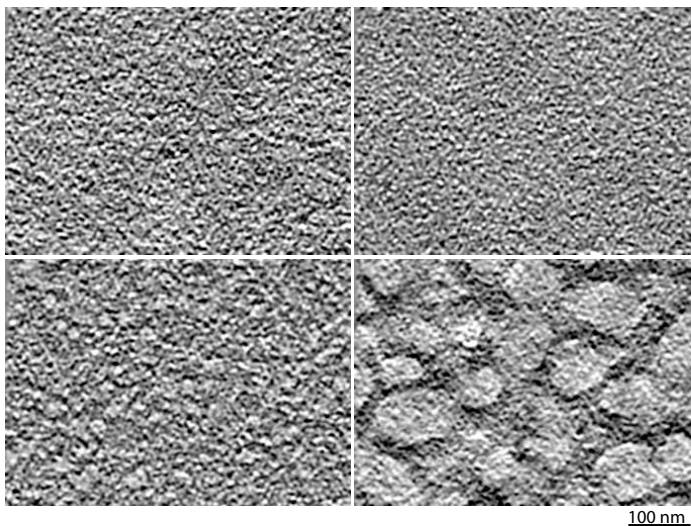
Figure 2.4: Middle sections (ca 1.6 nm thick) of tomographic reconstructions of APFO-3:$PC_{61}BM$ with different stoichiometries. From upper left to lower right: 2:1, 1:1, 1:2, and 1:4

the conjugated polymer APFO-3 is mixed with $PC_{61}BM$ in different ratios

and spin cast into films. The difference in morphology is clearly seen between the 1:4 blend and the others. A coarser film structure is found in the blend with highest amount of $PC_{61}BM$. This blend ratio is also the one giving the best performing devices. [59]

2.1 Morphology measurements

As the morphology of OSCs is believed to have a large impact on the function of the device much effort have been put into measurements and its description. Some techniques are more commonly used for that purpose, and are shortly described below.

Atomic Force Microscopy

Atomic force microscopy (AFM) is a well established technique for examination of surface morphology. [61, 62] Commonly when imaging the topography of a sample with AFM, an oscillating cantilever, with a small tip, is used. The cantilever and tip is moved over the sample, and the sample-tip interaction causes changes in the amplitude and phase of the cantilever oscillations. During scanning, the height of the cantilever is adjusted to minimise the changes in oscillation amplitude. The phase difference between the measured cantilever oscillations and the driving signal is measured simultaneously with the topographical data. The phase data provides information about differences in material properties, albeit without species identification. The curvature radius of the tip is a few nanometres. Thus, the technique provides the possibility to image both the topography of the sample and changes in material composition, with high resolution. There is generally no need for any special sample preparation as long as the surface of interest is free for investigation. The disadvantage is that only the surface, and not bulk properties, may be examined. A way to retrieve some information about the bulk is to cut the sample to lay bare a surface of the bulk. [62, 63]

In addition to topography and material composition variations, variants of AFM are used to image other properties of the specimen.

Conductive AFM   Conductive AFM (CAFM) may be used to map the electrical properties of the film. [64] In CAFM a biased tip is in contact with the sample and the resulting current is measured, with or without the presence of light. The result may e.g. be a map of local resistance or JV-curve.

Kelvin probe force microscopy The difference in work function be-
tween the tip and the sample may be used in Kelvin probe force microscopy
(KPFM) to map the sample workfunction, [64] which provides additional
knowledge of the material. As the tip and material are put in contact their
Fermi levels will align and an electric field form between tip and sample.
The voltage needed to counter this field is the measured output signal.
Commonly KPFM is done in non-contact mode nowadays, to improve sen-
sitivity. [64]

Secondary ion mass spectroscopy

To gain information about the active layer as function of depth, secondary
ion mass spectroscopy [44] has been used. Here, the sample is bombarded
with ions which mills the sample down. The secondary ions produced are
detected by their mass to charge ratio, and information of material composi-
tion is in that way provided. Additionally, the molecules may be isotopically
labeled, with e.g. ^{2}H, for higher spectroscopic precision. In imaging mode
the primary beam is rastered over the surface and the secondary ions uses
to build the image. The lateral resolution, when imaging surfaces in this
mode, can be a few hundred nanometres. [65]

X-ray scattering

X-ray diffraction can be used to study the crystallinity of a material. Infor-
mation about crystal structure and crystallite size is obtainable with this
technique. [66]

Near-edge X-ray absorption fine structure spectroscopy

A useful technique for determining stoichiometry close to an interface is
near-edge X-ray absorption fine structure spectroscopy (NEXAFS), [67–69]
where the absorption, as function of wavelength, is measured. After excita-
tion of the sample fluorescent photons or Auger electrons are ejected. The
mean free path of the Auger electrons is small, thus electrons generated
at a larger sample depth loose their energy and is not contributing to the
signal. Hence the surface sensitivity of the technique. In addition a retard-
ing electric field can be employed, so that only electrons from very close to
the surface is detected. This partial electron yield mode increase the sur-
face sensitivity even further, as compared to total electron yield detection,
where all available electrons are used. By varying the incidence angle of the
polarised wave, orientation of dipoles may be deduced.

Scanning electron microscopy

Another surface mapping technique is scanning electron microscopy, where an electron beam is focused to a diameter of a few nanometres and scanned over the sample. The incident beam interacts with the sample and electrons are scattered back, elastically and inelastically. The backscattered electrons are detected and this signal form the surface image. SEM has been used to image cross sections of donor acceptor blends of OSCs. [35]
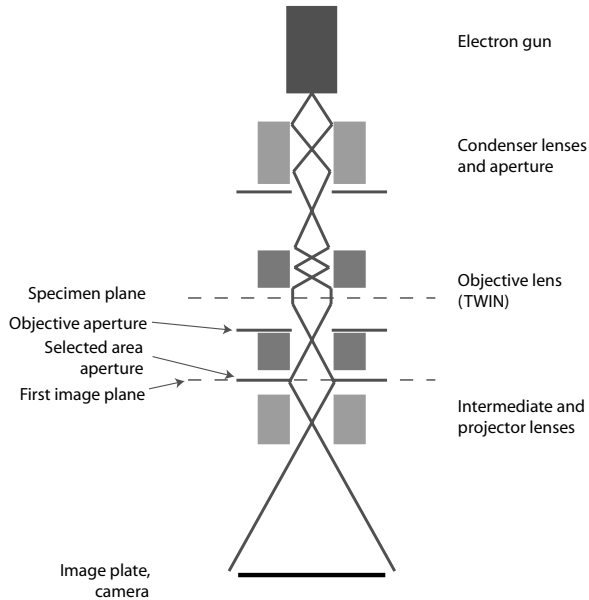
2.1.1 Transmission electron microscopy

The foundation of electron tomography is the images, obtained by transmission electron microscopy (TEM). Here electrons are used for image formation, as compared to photons in light microscopy. As the electrons are accelerated over several thousands volts their momentum will be high and (de Broglie) wavelength short. E.g. the wavelength of electrons accelerated over 200 kV is 2.5 pm. The short wavelengths enables a high resolving power.

A sketch of a TEM is found in figure 2.5, where the most important parts are depicted. Topmost in the microscope is the electron gun, of which there are several types. Thermionic and field emission guns (FEG) are two main categories. The thermionic gun consist of a filament under negative bias which is heated until emission of electrons occur. The electrons are sequentially accelerated by the electric field formed between the filament cathode and ground. A Schottky FEG is also heated, to nearly emit electrons. The FEG is connected to two anodes. The charges are emitted by an applied extraction voltage between the FEG (cathode) and the first anode. After that the charges are accelerated by a larger electric field, produced by the second anode. FEGs produce a higher current density and brightness than thermionic guns.

Right after the gun is a set of condenser lenses and condenser apertures. Two condenser lenses are commonly used, together with the pre-field objective lens (upper objective lens), to form a parallel electron beam at the sample position. The condenser aperture is here used to block a part of the electron beam and making it more parallel.

The objective lens is the most important lens in the microscope, as this forms the image of the sample. All errors associated with image formation are magnified further down the column. The objective lens is also the one most affected by aberrations, due to the large range of scattering angles. An objective aperture may be placed in the back focal plane of the lens to exclude electrons scattered at high angles, thus working as a lowpass filter and increasing contrast in the image. There is also a selected area aperture, placed in the image plane, used to select the area of interest when diffraction

Electron gun

Condenser lenses
and aperture

Objective lens
(TWIN)

Specimen plane

Objective aperture

Selected area
aperture

First image plane

Intermediate and
projector lenses

Image plate,
camera

Figure 2.5: Sketch of transmission electron microscope, including the most important features and the ray path, excluding electron-sample interaction.

is studied.

The objective lens magnifies the image around 50 times and the subsequent intermediate and projector lenses are used to magnify the image to the desired amount.

The image is projected onto a phosphorescent screen for viewing, or a camera for collection. Alternatively, the diffraction pattern, which is formed in the back focal plane of the objective lens, can be projected onto the viewing apparatus.

In figure 2.5 two electron rays are depicted as lines going from the electron gun, through various lenses, apertures and the specimen stage, ending up on the image plate. It is convenient, and most often sufficient, to think of the rays and action of the lenses as such. However, the electrons are charged species and the lenses electromagnets, so this picture is not entirely true. A significant difference between light microscopes and TEM is the rotating ray trajectory of the latter. As the electrons are subject to a Lorentz force the image will be rotated through the column, but can be compensated for by additional lenses.

Correction coils, used for the important alignment of the microscope

optics, are also omitted in figure 2.5 for clarity.

Image formation in TEM

In TEM electrons are used for collecting information of the specimen. Many of the incident electrons will pass through the sample unaffected, but some will be scattered, elastically or inelastically. Inelastic scattering is important for spectroscopic studies, such as X-ray or electron energy loss spectroscopy, where light emitted from the excited sample, or the energy loss of the transmitted electrons, are detected respectively. The detected energy distribution can be used to map the concentration of different elements.

A part of the elastically scattered electrons are deflected enough to be absorbed outside the objective aperture, contributing to the amplitude contrast, as illustrated in figure 2.6. With lighter materials, e.g. biomaterials or active layers of OSCs, most of the scattered electrons are deflected at a low angle, and thus transferred through the objective aperture. Still, these electrons carry information about the specimen by their change of phase, relative the unscattered electrons, and will contribute to phase contrast.
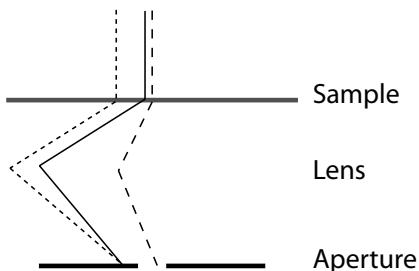
Figure 2.6: Schematic illustration of the objective aperture and its effect on scattered electrons. Electrons scattered at a sufficiently high angle are absorbed outside the aperture.

Phase contrast is due to the interference of electron waves. The waves before and after specimen and optics are depicted in figure 2.7. The incident plane electron wave, ψ_i, is scattered by the sample, and the scattered wave, ψ_s, may generally be described as [70–72]

$$\psi_s = f_s \psi_i = (1 - s) \exp(i\phi_s)\psi_i \tag{2.5}$$

where f_s is a specimen function, describing scattering as absorption and phase shift of the incident plane wave. The phase shift, ϕ_s, of the scattered
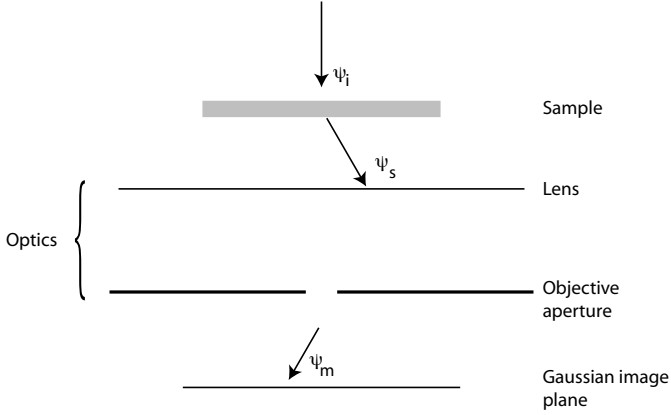
wave may be described by

$$\phi_s = \frac{2\pi}{\lambda} \int_{-\infty}^{\infty} (n(\boldsymbol{r}) - 1) dz = -\frac{2\pi}{\lambda E} \frac{E - E_0}{E + 2E_0} \int_{-\infty}^{\infty} V(\boldsymbol{r}) dz \qquad (2.6)$$

where

$$n(\boldsymbol{r}) = 1 - \frac{V(r)}{E} \frac{E + E_0}{E + 2E_0} \qquad (2.7)$$

is the refractive index [72], wherein E and E_0 are the kinetic and rest energies of the electrons, and $V(\boldsymbol{r})$ the potential in the material. This means that the phase change is proportional to the projected sample potential. The wave is transferred to the image plate/camera via electron optics and

Figure 2.7: Electron waves in the microscope. ψ_i is the incident plane wave, ψ_s the scattered wave and ψ_m the wave reaching the image plane.

as the scattered wave travels down the column it is phase shifted also due to imperfect lenses and defocusing. Spherical aberration is of importance here. Spherical aberration means that the focal length of the lens is not constant with the distance from the optic axis. The objective lens focus the rays passing the lens at a larger radius more, as illustrated in figure 2.8. The aberration causes the ray to deviate from its ideal path an angle $\Delta\theta_s \approx \Delta r/b = C_s\theta^3 M/b$. [71] In figure 2.8 $M = b/a$, $a \approx f$ and $\theta \approx R/a$, thus

$$\Delta\theta_s = \frac{C_s R^3}{f^4} \qquad (2.8)$$

where C_s is the spherical aberration, f the focal length of the lens and R the radius at which the ray is diffracted.
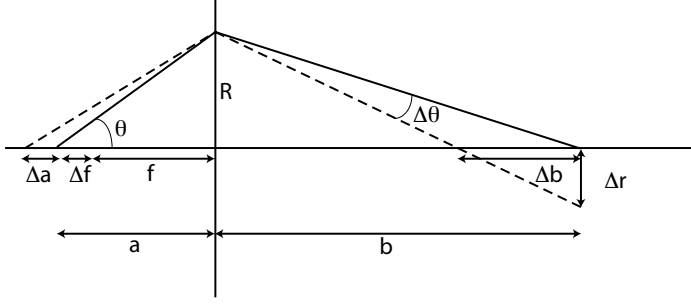
Figure 2.8: Angular deviation $\Delta\theta = \Delta\theta_s + \Delta\theta_a + \Delta\theta_f$, due to spherical aberration and defocusing.

Similar angular deviations may be achieved both by displacing the specimen a distance Δa and changing the focus value of the lens by Δf. With the use of the lens equation it can be shown that [72]

$$\Delta\theta_a = \frac{R}{f^2}\Delta a \tag{2.9}$$

and

$$\Delta\theta_f = -\frac{R}{f^2}\Delta f \tag{2.10}$$

The total angular deviation due to spherical aberration and defocusing is

$$\Delta\theta = \Delta\theta_s + \Delta\theta_a + \Delta\theta_f = C_s\frac{R^3}{f^4} - (\Delta f - \Delta a)\frac{R}{f^2} \tag{2.11}$$

The phase shift, due to aberrations and defocus, between two waves passing the lens at the optic axis and R, respectively is

$$\chi(\theta) = \frac{2\pi}{\lambda}\int_0^R \Delta\theta dR \approx \frac{\pi}{\lambda}(\frac{1}{2}C_s\theta^4 + \Delta z\theta^2) \tag{2.12}$$

where $R/f \approx \theta$ have been used and $\Delta z = \Delta a - \Delta f$. With the frequency coordinate $q = \theta/\lambda$, [72]

$$\chi(q) = \pi(\frac{1}{2}C_s\lambda^3q^4 + \Delta z\lambda q^2) \tag{2.13}$$

Returning to the general model for the description of the scattered wave, $\psi_s = f_s\psi_i$, and assuming a thin specimen, with only a small amount of scattering, the exit wave amplitude can be expanded to [70]

$$\psi_s = (1 - s + i\phi_s)\psi_i \tag{2.14}$$

The wave amplitude in the image plane, ψ_m is the convolution of the exit wave amplitude and the point spread function, $h(r) = \mathfrak{F}^{-1}(H(q))$, where H is the Fourier transform of h. That is

$$\psi_m = \psi_s * h = (1 - s + i\phi_s)\psi_i * \mathfrak{F}^{-1}(H(q)) \tag{2.15}$$

where $H(q) = \exp(-i\chi(q))P(q)$ is the contrast transfer function (CTF), including the function of the aperture, $P(q)$, but omitting the envelop functions, which describe the attenuation of the wave amplitude at larger frequencies. The image intensity is $\psi_m\psi_m^*$. If, since s and ϕ_s are small, quadratic terms are neglected, this becomes, with a normalised incident amplitude

$$I = \psi_m\psi_m^* = 1 - 2\mathfrak{F}^{-1}(SP(q)\cos\chi(q)) + 2\mathfrak{F}^{-1}(\Phi_s P(q)\sin\chi(q)) \tag{2.16}$$

where $S = \mathfrak{F}(s)$ and $\Phi_s = \mathfrak{F}(\phi_s)$.

s is usually small and phase contrast the dominant contrast mechanism, so the phase contrast transfer function, $A(q)P(q)\sin\chi(q)$, where $A(q)$ is an envelop function, may be used to extract the point resolution for a certain microscope and focus settings. The point resolution is found where the first zero of the CTF is located.

If the spherical aberration e.g. is 2 mm and the defocus is set to -2 μm, a point resolution around 2 nm is obtained, where the first zero of the CTF is found.

Along the optic path, between sample and image plane, apertures may be inserted. The most important aperture here is the objective aperture, situated close to the diffraction plane. As mentioned, this aperture acts as a lowpass filter, filtering out the waves scattered at large angles and thus large frequencies, improving the amplitude contrast.

3

Electron tomography

Tomography is a technique used to display the three-dimensional structure of an object. Commonly the structure is reconstructed from the combination of several two-dimensional projections of the object. A well known form of tomography is X-ray tomography, or computed tomography (CT), where X-rays are used to record projections of the sample. The technique is widely used in medicine.

Projections of a specimen is described by the Radon transform [73]

$$\check{f}(p, \theta) = \mathfrak{R}(f) = \int_L f(x, y) ds \tag{3.1}$$

which is the projection of a function f, as is illustrated in figure 3.1. The Radon transform and Fourier transform are closely related. It is seen that the Fourier transform of a projection equals the middle section of the Fourier transform of the projected function, as illustrated in figure 3.2a, in the discrete case. As θ is changed, Fourier space is filled and may be used for reconstruction of the full function f. [74, 75] In reality, time and sample stability limits the angular step size to some finite value, $\Delta\theta$, usually around one degree. This, together with the finite resolution of the recording medium, means that Fourier space is discretely sampled. In the case of thin films there is also a maximum possible tilt angle, which introduces a missing wedge of information, as illustrated in figure 3.2b. In practice other reconstruction methods than Fourier methods, such as weighted backprojection (WBP), arithmetic reconstruction technique (ART) or simultaneous iterative reconstruction technique (SIRT) is used for the reconstruction for computational reasons. WBP has been used in the work described in this thesis. Here, the backprojection is performed by respreading the projections over the volume. [76] The backprojection is convolved with the weighting filter, being the inverse of the transfer function of the backprojection. In
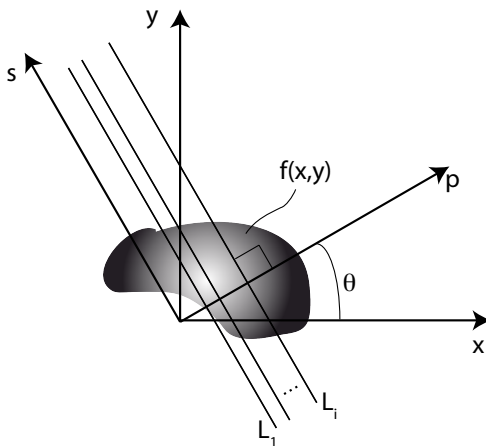
Figure 3.1: The two dimensional Radon transform of f is the collection of integrals of f along paths L_i, i.e. the projection of f.

two dimensions this is

$$f(x,y) = \mathfrak{F}^{-1}(B(q_x,q_y)W(q_x,q_y)) = \mathfrak{F}^{-1}\left(\frac{B(q_x,q_y)}{H(q_x,q_y)}\right) \qquad (3.2)$$

where $B(q_x,q_y)$ is the Fourier transform of the backprojected function and $H(q_x,q_y)$ the transfer function of the backprojection method.

In electron tomography (ET) [77] TEM is used for data collection, with the potential for higher resolution. The technique has been used for some time in biology for the study of virus and cell structures, [78–80], and in material sciences [75], e.g. polymer science, for visualisation of copolymers and blends. [81–86] It has more recently been applied to OSC materials, [34, 53, 87–97] which are similar to biomaterials in the sense that they are soft materials, mostly consisting of carbon. They are also fairly sensitive to electron radiation, which limits the exposure and the signal to noise ratio, even though the solar cell materials tend to be more robust than biological samples.

In ET, the resolution of the final reconstruction is limited by the tilt angle step. According to Crowther's criterion, [76, 98] the resolution, d, is limited to

$$d = D\Delta\theta \qquad (3.3)$$

where D is the typical feature size and $\Delta\theta$ the tilt angle step size. Using the film thickness of 100 nm as the typical feature size and a tilt angle step of $1°$ gives a resolution $d=2$ nm. This resolution estimate has been

q_y

q'_y

q'_x

θ

q_x

q_y

q_x

(a)

(b)
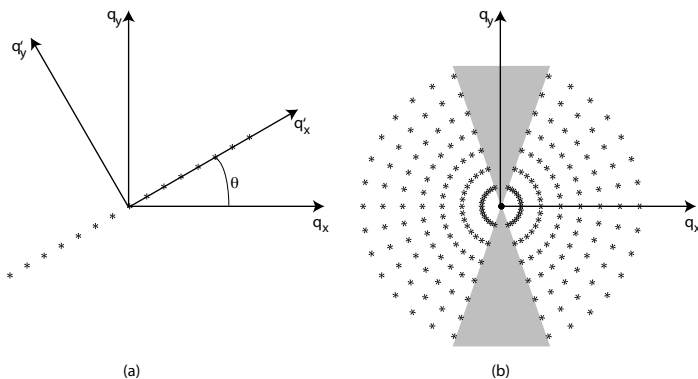
Figure 3.2: (a) Sampling of Fourier space by projections. (b) Discrete sampling from multiple tilt angles, illustrating the effect of the missing wedge. $*$ indicate sampled function points.

shown to sometimes be too conservative. [99, 100] The sampling frequency is not the only resolution limiting factor in ET. For organic materials the low signal to noise ratio has a severe impact on the final result. One way of assessing the resolution of tomography reconstructions is Fourier shell correlation (FSC), [101] where two reconstructions are made; one for each half set of angles. Their Fourier transforms are compared and the correlation as function of spatial frequency is used for resolution estimates. To define one resolution value from the FSC is however not straight forward, and several suggestions to that exist. [102]

3.1 Electron tomography of organic solar cells

Active layers of OSCs are suitable for morphological studies by ET, as their thickness is typically small enough. The active layer need to be detached from the other layers of the cell. One way of achieving this is to utilise the water solubility of PEDOT:PSS, typically used as anode in OSCs. When the active layer has been prepared, without cathode, the substrate is immersed in water to dissolve the anode, leaving the layer of interest floating. Alternatively, complete solar cells may be used by selecting the film close to the metal cathode. The floating specimen is picked up by a copper grid, and gold nano particles are placed on the surface, as indicated in figure 3.3. The well scattering Au-particles are used as help in image alignment in the later reconstruction step. At this stage the sample is ready for data collection.

Data collection is performed in a TEM which allows for high tilt of the
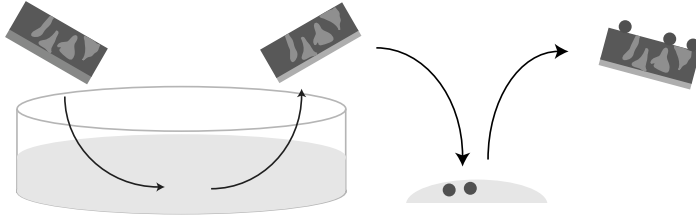
Figure 3.3: Sample preparation of tomography specimen. PE-DOT:PSS is dissolved, leaving the active layer on the water surface. The film is picked up with a Cu-grid and exposed to a gold particle containing solution.

sample holder, and is nowadays greatly facilitated by computer controlled microscopes, allowing for automatic adjustment of tilt angles, focusing, image tracking and exposure. During data collection the sample is typically tilted from ca -70° to ca 70°, in steps of around 1°. Since the specimen is never completely flat or stable there is a need for image tracking and refocusing during the procedure. In figure 3.4 are examples of images at high and low tilt angle, recorded during data collection. The lack of clear
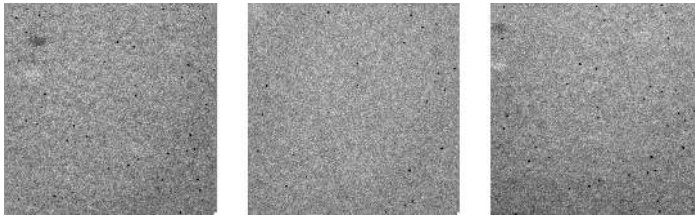
Figure 3.4: Examples of typical images obtained during data collection at high and low tilt angles. Image width is ca 1.5 μm in the specimen plane. Tilt angles are -60°, 0° and 60°.

features, due to the low contrast, can be noticed in these images.

Following data collection the projections are aligned, with the help of the applied Au-markers. As these scatter electrons very well, they are easily distinguished from the rest of the film. Even so, there is commonly some alignment imperfections leading to a diminished resolution in the final tomograms. An area of interest is thereafter extracted, and these images are used for the data reconstruction. The work in this thesis has been performed in close collaboration with Karolinska Institutet, Stockholm, Sweden, where

data collection has been performed and from where software for the reconstruction steps has been used.

Most of the polymer and fullerene consist of carbon. With this follows a low contrast in the TEM images and reconstructions. However, there is sufficient contrast between the polymer and the fullerene to produce images useful for tomography. Another problem with visualising the blend is that the phase formation involves mixing of the two materials. [51] Since the resolving power of the microscope is too poor to distinguish the different species in the mixed phases, the phases can only be differentiated as polymer rich and fullerene rich. The film formation, when using e.g. spin coating and volatile solvents, results in films away from equilibrium, so the phase diagrams of polymer:fullerene blends cannot be straightforwardly used to gain knowledge about the local stoichiometries in the sample.

Even with the aforementioned difficulties ET has proven beneficial in the work with OSCs. Especially the comparison of similar samples, differing in preparation method or solvents used, has been useful. [34, 53, 88, 89] The polymer HXS-1 [41] blended with $PC_{71}BM$ is a good example of this. The effect of adding a small amount of 1,8-diiodooctane (DIO) to the main solvent, ortho-dichlorobenzene, was seen as a larger J_{sc} and FF as compared to solar cells prepared without DIO. [34] From tomography studies it could be seen that the active layers prepared with the use of DIO showed a coarser morphology than the layers made without the extra solvent, as seen in figure 3.5, where planar sections close to the middle of the reconstructed films are displayed. During analysis of the reconstruction several different lowpass filters and thresholds are used to assess the morphology and compare this to the morphology of other samples. Thus, there is much visual inspection involved in the analysis, but for simple presentation and comparison of the morphology of materials, the reduction of the reconstructions to data describing the morphology is desirable. This can be lengths [92], feature angles [93], aggregate volume [82] or crystallite density [89]

To further analyse the reconstructions and facilitate the comparison of materials and preparation techniques, it is desirable to extract some condensed measures of the morphology. When analysing tomography reconstructions, such as in figure 3.5, extraction of data can be performed in different ways. As domain sizes are of importance for charge formation and extraction a measure of that feature is desirable. Commonly the reconstructions are binarised to simplify the measurements. [92, 93] Binarisation is done by choosing a threshold and setting all voxels above this threshold white and the others black. Volumes, areas and distances may easily be measured in the resulting black and white images. The choice of threshold has, however, a large impact on the result of such analyses, especially in low contrast samples. Higher contrast samples, e.g. blends of organic
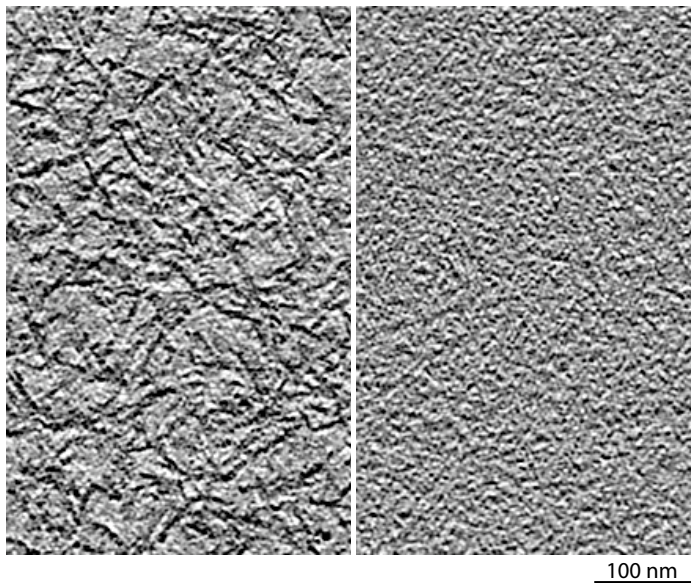
Figure 3.5: Planar sections ($\approx$1.6 nm thick) of HXS-1:PC$_{71}$BM with (left) and without (right) DIO. Reconstructions are lowpass filtered at 5 nm period.

materials and metal or metal oxides, makes the procedure easier, albeit far from trivial, and such reconstructions have been used to model the charge generation in the bulk. [92, 97] To this comes the noise reducing lowpass filtering, which also affects real data. Examples of the combined effect of the two image operations is found in figure 3.6, where sections of a reconstruction of HXS-1:PC$_{71}$BM (2:5), made with DIO, lowpass filtered and binarised at different thresholds, are shown. These images can be compared to images in figure 3.7 from reconstructions of HXS-1:PC$_{71}$BM (2:5), made without DIO, filtered and binarised in the same way. Even though the image processing produces images, from the same data, which are somewhat dissimilar, the difference between the two samples (with and without DIO) is still clear. The sample prepared with the use of additional DIO exhibit a coarser structure compared to the other sample.

These examples elucidate the difficulty of choosing one binarisation threshold for further morphology description. It may be argued that a threshold giving the correct volume ratio should be used for binarisation, but since it cannot be stated that the phases are pure, the solution is not as straightforward. Due to this, the analysis in this work has been performed with the
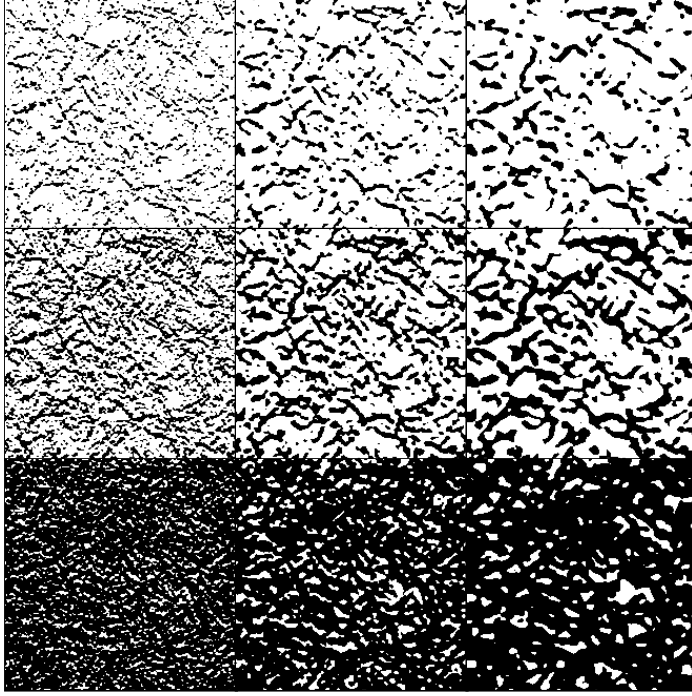
Figure 3.6: Planar sections (≈1.6 nm thick) of HXS-1:PC$_{71}$BM (2:5) from solvent with DIO. Lowpass filtered at (from left to right): 5 nm, 10 nm and 15 nm period. Binarisation, from top to bottom, at threshold 0.2, 0.4 and 0.8. Sections are 345 nm wide.

use of multiple thresholds. Measurements of interest have primarily been the distance from an arbitrary point to the nearest interface and the interface area, due to their importance for charge generation and extraction. From binarised reconstructions length values can be extracted by the use of a distance transform, where the voxels in the volume are mapped onto a volume with the shortest distance to a black-white interface. From here mean values of distances in the two phases may be extracted, for example. Interface areas are also easily extractable from the same binarisation of the data. As stated this is done for volumes binarised at several thresholds. Thus, each reconstruction gives a vector of numbers, which can be used to compare active layers. Such a comparison of mean distances from within the phases to the nearest interface is shown in figure 3.8, where films of HXS-1:PC$_{71}$BM (2:5) made from solvent with or without additive are compared.
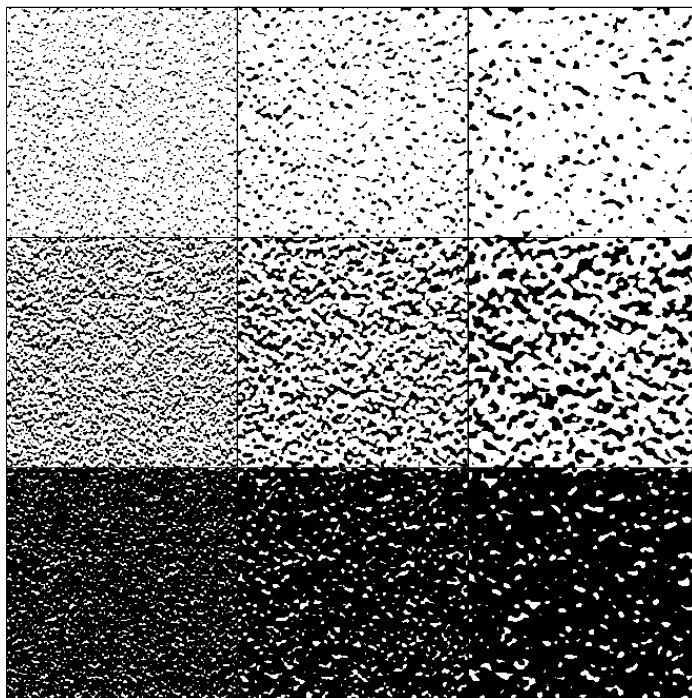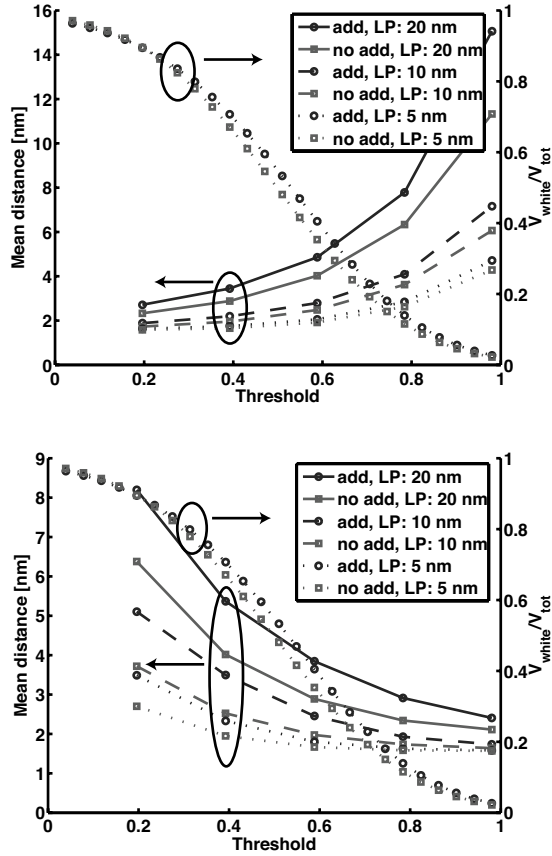
Figure 3.7: Planar sections (≈1.6 nm thick) of HXS-1:PC$_{71}$BM (2:5), from solvent without DIO. Lowpass filtered at (from left to right): 5 nm, 10 nm and 15 nm period. Binarisation, from top to bottom, at threshold 0.2, 0.4 and 0.8. Sections are 345 nm wide.

Figure 3.8: Mean distance from every black (upper) or white (lower) point to the nearest interface in binarised reconstructions of HXS-1:PC$_{71}$BM (2:5), from solvent with or without DIO. The ratio between the volume of white points and the total volume is also shown.

The result is shown for several thresholds and for three lowpass filters. The difference is not large between the results from reconstructions lowpass filtered at 5 nm period, which is probably due to the low signal to noise ratio. The impact of noise on the result is therefore large with these settings. Nevertheless, the data from reconstructions filtered at 20 nm show a larger difference, corresponding to the coarser morphology of the sample prepared with solvent additive (see figs 3.6 and 3.7). Care must however be taken during such analyses. Even if the magnification is kept at a moderate level during data collection, the sampled area is still small compared to the total solar cell. E.g. in figure 3.9 are reconstructions of a TQ1:PC$_{71}$BM (1:2). [103] The properties of solar cells made by spincoating this blend was found to be dependent on the distance between the cell and the rotation centre. [53] Figure 3.9 display planar sections of reconstructions of films taken about 12 mm and 1 mm from the rotation centre, respectively. Two different magnifications have been used in both cases. The coarser structure of the

100 nm
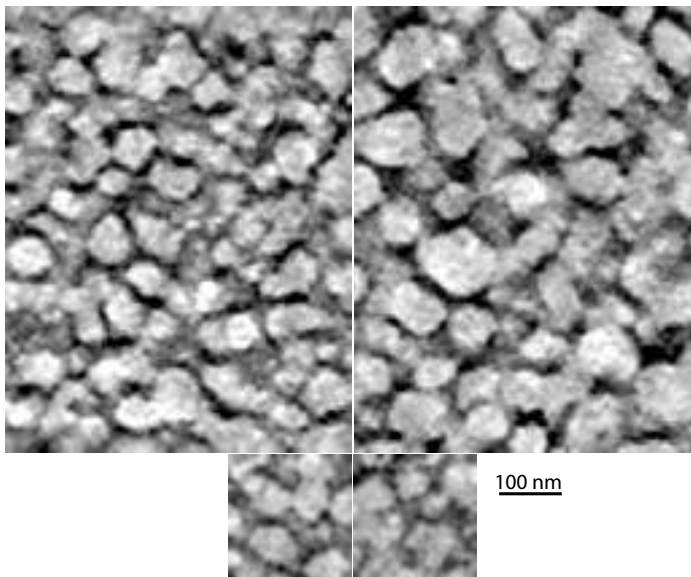
Figure 3.9: Planar sections of TQ1:PC$_{71}$BM (1:2). Samples taken ca 12 mm (left) and ca 1 mm (right) from the rotation centre. Data collection performed at 20 kx magnification and single tilt series (upper) and 50 kx magnification and double tilt series (lower). Lowpass filter at 20 nm has been applied.

film taken 1 mm away from rotation centre, as compared to the film from 12 mm, is obvious in the reconstructions from lower magnification. The

difference between the other images, from higher magnification, is not that clear. Here are only a handful of the lighter blobs seen, compared to nearly ten times as many in the case with lower magnification. The use of these reconstructions for distance measurements also give different results, as seen in figures 3.10 and 3.11.
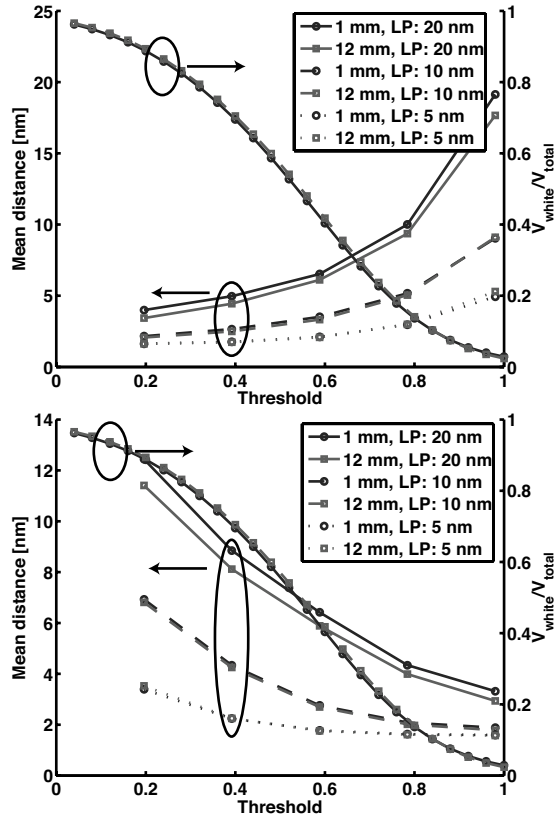
Figure 3.10: Mean distance from every black (upper) or white (lower) point to nearest interface in binarised reconstructions of TQ1:PC$_{71}$BM (1:2). Calculations are done using data collected at 20 kx magnification. The ratio between the volume of white points and the total volume is also shown.
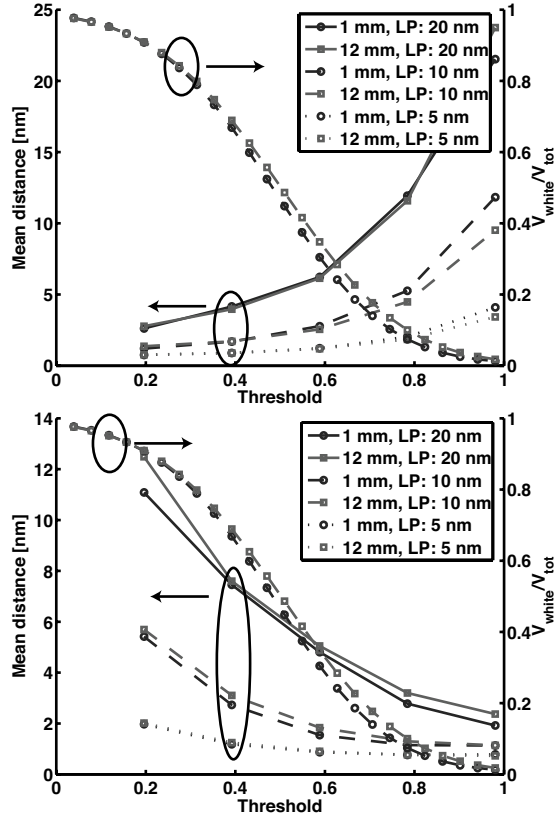
Figure 3.11: Mean distance from every black (upper) or white (lower) point to nearest interface in binarised reconstructions of TQ1:PC$_{71}$BM (1:2). Calculations are done using data collected at 50 kx magnification. The ratio between the volume of white points and the total volume is displayed as well.

The result from the reconstructions from lower magnification (fig 3.10) harmonise with the apparent morphology difference seen in the upper part of figure 3.9. In figure 3.11 the difference is very small and even indicate the opposite coarseness relation between samples. The reason for this could well be that the smaller sampling volume used does not accurately represent the morphology of the active layer. Thus, as with two-dimensional TEM measurements, care need to be taken during ETOM measurements and analysis so that an appropriate area of interest is studied. This may be difficult to achieve without knowledge of the inner structure, which is often revealed only after reconstruction, due to the low signal to noise ratio.

The comparison of morphologies and device performance shows that a larger current density is associated with a coarser morphology in the case of HXS-1:$PC_{71}BM$, while the opposite is the case with TQ1:$PC_{71}BM$. This is an indication of the complex process of current generation in OSCs, where exciton quenching, recombination and transport are important properties which should be mutually optimised and may depend on morphology. These properties affect the IQE, which can be estimated by comparing the measured EQE with results from optical modelling. A comparison that shows that the IQE is indeed higher in the better performing devices.

Due to the limited tilt angle, imposed by the geometry of the thin film samples and sample holder, there is a missing wedge of data in the q_z-direction of frequency space, as discussed above. This means that frequencies corresponding to structures parallel to the film surfaces and orthogonal to the tilt axis are badly sampled, with following artefacts, such as elongation of features in the z-direction. A way of reducing the amount of lost data is to perform an additional data collection with the rotation axis orthogonal to the first. In addition to an increase in the number of images, the missing wedge is reduced to a missing pyramid, with improved image quality as a result. [83, 104, 105] The difference between reconstructions of data from single- and double tilt is exemplified in figure 3.12, where a middle section of a sample of iron decorated amyloid fibrils [106] is shown. The left hand image is reconstructed from data from one tilt axis, while two orthogonal axes of rotation have been used for the right hand image. Though the difference between the images is small, some fibres are better rendered in the image from double tilt. These are fibres lying in a direction close to orthogonal to the tilt axis in the single tilt case, and thus corresponding to frequencies lying in the missing wedge.

The introduction of Fe-particles could cause problems with reconstructions due to the crystalline nature of the particles. Electron diffraction in crystals cause angle dependent intensities in the sample data, which can introduce artefacts in the reconstructions. However, since the effect of scattering is large only at a small number of angles, the final reconstruction is
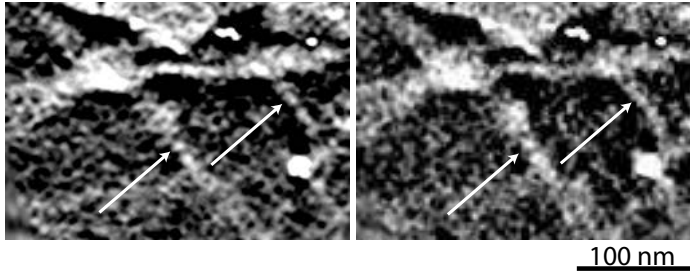
Figure 3.12: Sections of a reconstruction of amyloid fibrils decorated with Fe-particles. Left image is from single tilt, with the tilt axis horizontally. Right image is from double tilt. Reconstructions are lowpass filtered at 10 nm. Two fibres are indicated by the arrows.

usually almost unaffected, [107–109] due to the averaging effect. The same thing is seen in the reconstructions of the iron decorated amyloid fibres. The collected data does show an intensity oscillating with the tilt angle, but the final reconstructions do not show iron particle shapes deviating from the expected.

4

Optical modelling

New materials for OSCs are constantly synthesised, with the aim of improving properties like light absorption, photovoltage, durability and charge transport. New materials bring new optical properties, which affect the absorption and reflection of the solar cell. Also, the use of novel device structures, such as the removal of indium tin oxide (ITO) as charge transporting layer, involve alterations of layer sequences and thicknesses. As the layers of the OSC is typically around 100 nm the optical behaviour is governed by interference effects, and it can thus be difficult to foresee the effect of device structure changes. In figure 4.1 is the simulated result of the number of photons absorbed in three devices shown. Here, the electric fields are calculated with the transfer matrix method (TMM), [110–112] and number of absorbed photons is calculated from the E-field. TMM is a common and useful technique for calculation of the electric field within a one-dimensional stack of thin, planar, layers. The modelling is done by considering reflections and transmissions at all interfaces in the modelled stack. By superimposing waves travelling down and up the stack, and considering the attenuation due to absorption within each layer, the total electric field is found. The absorbed energy at a point in the stack is proportional to the square of the electric field, as [110]

$$Q(z, \lambda) = \frac{1}{2} c \epsilon_0 \alpha n(z, \lambda) |E(z, \lambda)|^2 \qquad (4.1)$$

where c is speed of light, ϵ_0 permittivity, $n(z, \lambda) = \mathfrak{Re}(\tilde{n}(z))$ the real part of the refractive index and

$$\alpha = \frac{4\pi k(z, \lambda)}{\lambda} \qquad (4.2)$$

where $k(z, \lambda) = \mathfrak{Im}(\tilde{n}(z, \lambda))$ is the extinction coefficient and λ the wavelength. Thus, the number of absorbed photons and maximum photocur-
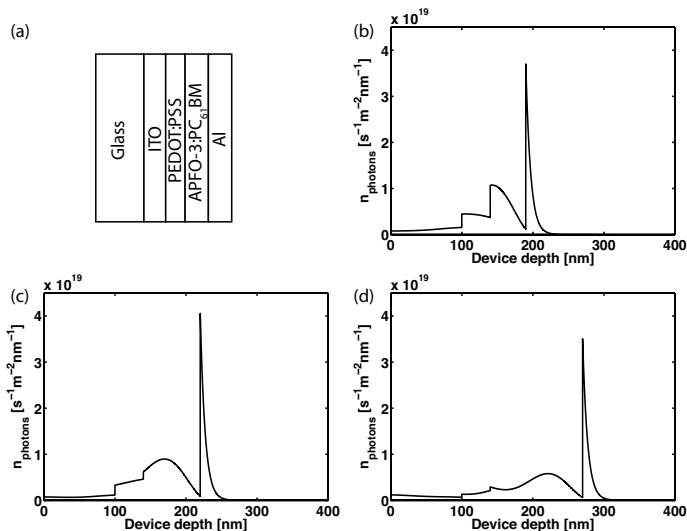
Figure 4.1: Structure of device modelled with TMM (a) and number of absorbed photons (glass omitted) for three active layer thicknesses. Device structure is: glass, ITO (100 nm), PEDOT:PSS (40 nm), APFO-3:PC$_{61}$BM, Al, with active layer thicknesses of 50 nm (a), 80 nm (b) and 130 nm (c).

rents, where an IQE of unity is assumed, are easily calculated.

As seen in figure 4.1, the change of active layer thickness have a significant effect on the absorption profile, which make the absorption, and electric field, profile important for the device functionality. Much light should be absorbed in the active layer, while the absorption in electrodes and reflection should be kept low, for high currents. The maximum possible photocurrent may be calculated by neglecting any electrical losses and assuming that every photon absorbed in the active layer gives rise to an electron in the outer circuit. This means no charge recombination, and thus $\eta_{IQE} = 1$. The maximum photocurrent versus active layer thickness is shown in figure 4.2, which exemplifies the active layer thickness dependence on absorption and photocurrent generation. A local maximum is found around 80 nm active layer thickness for this configuration. Such a local maximum is typical and point to the importance of optical modelling in the field of OSCs. Calculating the optical effects of device structure changes is easier and faster than building devices. It can also be useful to isolate optical effects in the analysis of new materials or devices.

Not included in this thesis, but essential for optical modelling, is the
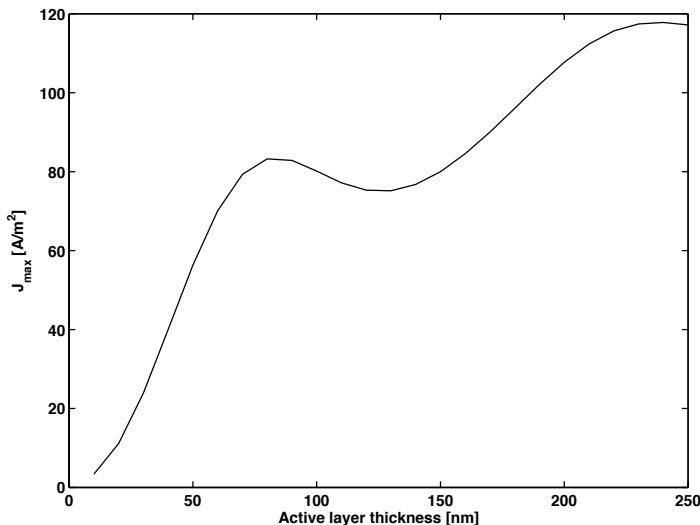
Figure 4.2: Maximum photocurrent as function of active layer thickness. Device structure is: glass, ITO (100 nm), PEDOT:PSS (40 nm), APFO-3:$PC_{61}BM$, Al.

obtention of input data in the form of refractive indices. This is has been done using variable angle spectroscopic ellipsometry, where the change of polarisation of light upon reflection is used to determine properties of the sample. The sample is in this case a layered stack of materials, and properties such as thicknesses and refractive indices may be extracted. Here the film morphology affect the optical properties. Especially in the case with pure polymer films the chains has a tendency to line up with the substrate, giving an anisotropic refractive index. [113] An effect which can be highly dependent on preparation method and conditions, [114] and in bulk heterojunctions it can be seen at a variable degree. [111, 115] Due to this the refractive index of a blend depends not only on the stoichiometry, but also on the morphology resulting from the mixing. Attempts to apply an effective mean field approximation (EMA) to describe the refractive index of the blend as a combination of the indices of the neat materials have been made. There is no general good fit between EMA and measured data, however. [111, 115] Thus, there is a need to establish the optical properties with the stoichiometry of interest, which may mean that several blend ratios need to be prepared and measured.

The advantage of utilising optical modelling when optimising OSCs is associated with the electrical properties of the materials. A common current

problem with organic electronic materials is the low light absorption as compared to the charge transport. Thus, the active layers of organic solar cells need to be thin to allow for good enough charge extraction. Too thin layers are, however, not good from a light absorption point of view. The bad charge transport properties also implies the need of a transparent electrode, to minimise the charge transport distance within the active layer. Thus, organic solar cells are thin film stacks, and as such heavily affected by interference.

The use of multiple active materials, in tandem cells, is a way of reducing energy losses associated with thermal relaxation of excitons formed by short wavelengths of absorbed light. Optical modelling has shown to be useful here, as current matching of the subcells is often needed. This is when the subcells are connected in serial, which is common for stacked tandem solar cells. Serial connection is also good for diminishing resistive losses. In addition, the potential photocurrent should be maximised with the materials at hand. This is a complex task for which optical modelling has proven useful, [116] especially since the optimal structure, in the optical sense, may involve the low bandgap cell closest to the sun. [117–119] This may be unintuitive considering the description of tandem solar cells as filters and absorbers (see fig 1.8), but is a result of the thin layers used in OSCs. Thicker layers would show a Beer-Lambert like absorption and small internal reflections.

Different kind of techniques for enhancing the absorption without affecting the transport properties have been studied. These include the use of diffraction gratings to couple the light into the active layer, [13, 120] or producing surface plasmons to locally increase absorption. [121] Nanoparticles have also been used to produce plasmons and scatter light to improve absorption in both inorganic and organic solar cells. [122] External light trapping features, such as lenses [123] or fluorescent absorbers [18] have been applied to OSCs as well. Mirroring structures to confine the light have also been studied. [12] An efficient light trapping configuration which is possible to produce in large format is the folded solar cell, or V-cell. [14–17] Here two solar cells are placed facing each other in a V-shaped configuration. Alternatively, a softer substrate is used and folded to produce the same kind of structure. [124] In figure 4.3 is a sketch of the V-cell found. Two rays showing the reflection at the first interface are included in figure 4.3 to indicate the combined light trapping and energy filtering effect found in the structure. Light which is not absorbed by one of the subcells is available for absorption in the other cell. This is repeated a number of times, depending on the folding angle, α. Thus the optical path length is enhanced without enhancing the charge extraction path length. If the absorption properties of the individual subcells are dissimilar, an additional filtering effect is ob-
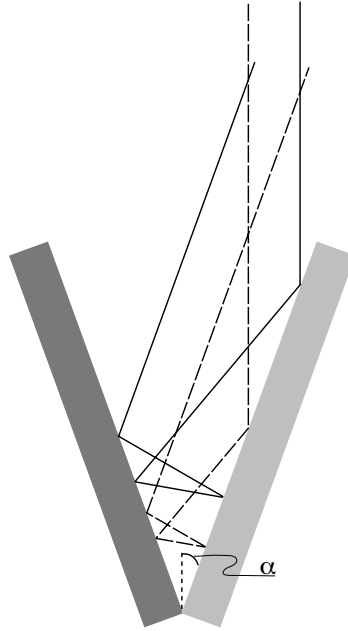
Figure 4.3: Simplified sketch of folded cell (V-cell). The principle of multiple reflections and the definition of folding angle, α, is shown.

tained, resulting in a tandem cell. In a stacked tandem solar cell transparent electrodes or recombination layers are needed to allow the light to reach the subcell furthest from the sun. In a stacked, serial connected, solar cell the recombination layer may be formed in various ways, including thin metal or metal oxide layers [125–127], which can be combined with an organic material. [118, 128, 129] As the subcells of the V-cell may be prepared separately or side by side and then folded together to form the final configuration, the need of a transparent cathode or recombination layer is absent.

TMM is efficient for the modelling of one-dimensional structures. Modelling of the V-cell requires calculations in two dimensions, incorporating several, oblique angles of incidence. Non-normally incident light may be problematic to handle with TMM. [130] For these calculations the finite element method (FEM) has been utilised. Here the area (or volume) of interest is subdivided into a fine triangular mesh. A set of trial functions is defined such that each function, v_i, equals 1 at the vertex numbered i and equals 0 at all triangles not touching the i:th vertex. There is thus N trial functions in the set, where N is the number of vertices in the triangulation.

The solution to the differential equation, for function u,

$$F(u) = f \qquad (4.3)$$

is approximated by a linear combination of the trial functions, v_i [131]

$$u_{approx} = \sum_{i=1}^{N} U_i v_i \qquad (4.4)$$

where the coefficients U_i are sought. By applying a variational formulation of the problem, for u_{approx}, an equation system with the unknown U_i is obtained. [131, 132]

The application to electromagnetic waves is implemented in COMSOL MULTIPHYSICS, where models are built by specification of the geometry and dielectric functions of materials. Maxwell's equations are then solved over the specified geometry. Thus, interference and reflections are considered in the calculations, together with the propagation of light in several directions within the multilayer stacks. This makes the method suitable for investigation of the optical properties of the V-cell.

For accurate calculations, the triangle mesh need to be fine enough. Around five vertices per wavelength is often stated as a rule of thumb, and by comparison with modelling results from TMM of planar structures the acceptability of the mesh size can be verified. As the number of unknowns in the equation system grows quickly with the size of the modelled structure, this need to be kept small to minimise computing time and memory use. For the V-cell this means keeping the legs of the V short. On the other hand, too small features may introduce undesired interference and diffraction effects not found in the real, mm-scale, system, and for this reason the geometry needs to be large enough. This was tested by comparing results from modelled V-cells with different leg lengths, but otherwise identical properties, to find a length where the results are stable to changes in length. [17]

Once the geometry is defined the problem is solved, for all wavelengths of interest, to gain the electric field at all points in the structure. To achieve knowledge about the effect of folding angles and layer thicknesses several geometries are used for calculation and since the these are performed in two dimensions they require longer time compared to modelling done with TMM.

4.1   Optical modelling of devices

Usually, the current per area is considered when optimising devices, as seen in figure 4.2. However, if cost of materials is cause for concern the current

per active layer volume should be considered. The aperture area of the V-cell is decreased with the folding angle, causing an increase of volume of material used per area. Figure 4.4 shows the maximum photocurrent per volume of active layer from an APFO-3:PC$_{61}$BM device. Several active layer thicknesses and folding angles are shown. Interestingly, there is a local maximum around 40 nm active layer thickness and a 50° folding angle, giving slightly higher current values than the planar cell with equal thicknesses. The active layer volume of the V-cell, at $\alpha = 50°$, is ca 1.3 times larger than the corresponding planar cell. Even so, the effect of light trapping is slightly larger than this here. When the cell is folded to $\alpha < 60°$ the light trapping
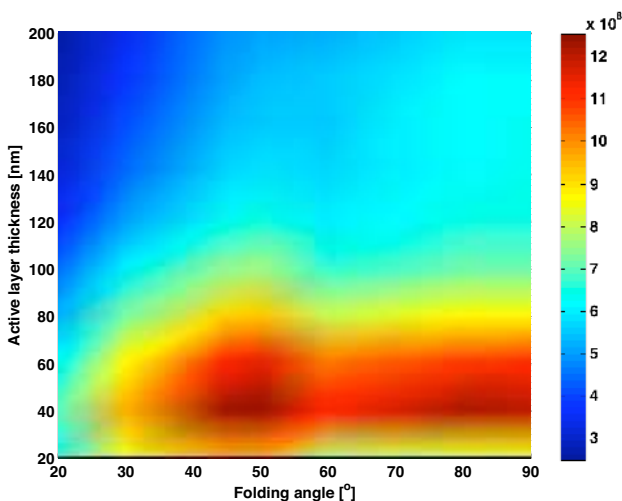
Figure 4.4: Maximum photocurrent per active layer volume [A/m^3], as function of folding angle and active layer thickness. The cell structure is PEDOT:PSS (40 nm), APFO-3:PC$_{61}$BM, Al.

effect start to manifest itself. For higher angles the light is reflected away at the first bounce. This is the reason for the increase in current per volume seen at these angles. As the cell is folded to even smaller angles the increase in current density is smaller than the increase in volume so the values decrease here. The situation is somewhat different in the case of tandem cells. Here the ratio of active layer volumes is $V_{act,V}/V_{act,P} = (2\sin(\alpha))^{-1}$ for equal total layer thicknesses, i.e. $d_{tot} = d_{cell1} + d_{cell2}$. This means that the material usage is smaller in the folded cell for folding angles above 30°, but increases sharply with diminishing angles. The optical behaviour of tandem cells, both in folded and planar configuration, was studied in ref 117, where

the maximum photocurrent of serial connected cells was considered. In serial connected cells the currents from the subcells should be balanced, so the active layer thicknesses need to be tuned to achieve this. The comparison of maximum photocurrent as function of total active layer thickness yielded the conclusion that the folded cell was able to deliver comparably high currents. The material usage was however not discussed. This can be taken into consideration by plotting the current density as function of active layer volume density instead of total thickness. The active layer volume density is defined as active layer volume per cell area. The resulting current densities are shown in figure 4.5. The active layer volume density for the planar cell
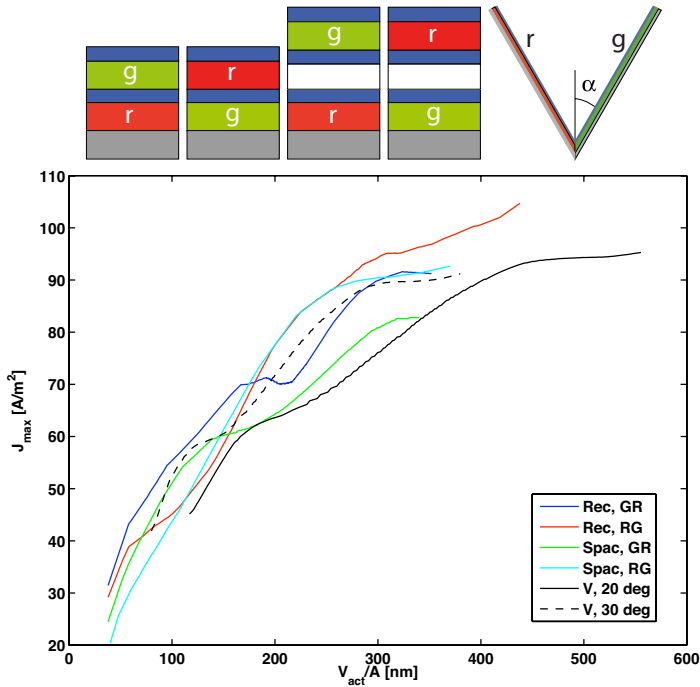
Figure 4.5: Maximum photocurrent for different active layer volume densities (V_{act}/A), for tandem cells. The cell structures are shown at the top, where g stands for APFO-Green5:$PC_{61}BM$ and r for APFO-3:$PC_{61}BM$. From left to right: Rec GR; Rec, RG; Spac, GR; Spac, RG; V-cell.

is the same as the total thickness, whereas it is increasing with decreasing folding angle for the folded cell. E.g. a V-cell with a folding angle of 20° exhibits a volume density 1.5 times higher than a planar tandem cell with

the same total active layer thickness. However, a 30° folding angle gives the same volume density as a corresponding planar tandem cell. Thus, the current density is larger for the more open 30° cell than for the 20° cell, when compared in this manner, in contrast to the case where only thicknesses are compared.

An OSC should be able to cope with many light incident angles, if a tracking system is not used, which should be avoided to keep costs low. The expected maximum energy output from tandem solar cells in folded and stacked configuration, during one summer day, was calculated and compared. [133] It was found that the folded cells where able to absorb more light than the planar cells during the day. It was also found that there may be difficult to achieve balanced currents during all of the day by simple active layer thickness adjustments.

Since light absorption in OSCs is much influenced by interference, addition of thin layers in the stack affects the active layer absorption and photocurrent. It has been suggested that the addition of an optical spacer between the active layer and the reflecting cathode could have beneficial optical effects. [134–136] By introducing this extra layer the electric field, and absorption, inside the active layer is changed. An idea is to improve the device optically by such an extra layer. However, it was shown that, for several materials, a positive optical effect could only be achieved if an active layer thickness away from a local absorption maximum was chosen. [137] The addition of an interface layer can have other beneficial effects, depending on spacer material. The spacer may work as a hole blocking layer to decrease interface recombination, or a rough layer which may have additional scattering properties which result in increased absorption and photocurrent. Since there is a positive effect seen for active layers thinner than optimal, an optical spacer can be used to enhance the photocurrent while maintaining a thin layer, which may improve charge extraction.

4.

5

Summary of work

The work in this thesis includes both morphology measurements of organic solar cell materials with the use of electron tomography and modelling of the optical behaviour of devices with different geometries. The included articles are summarised below.

5.1   Paper 1

As electron tomography is a fairly new tool for OSC studies the primary aim has been to establish the technique and try to understand its possibilities and limitations within this field. Although the blended materials typically used in OSCs are similar, the contrast obtained in TEM was found to be large enough to produce tomographic reconstructions with morphology information in three dimensions. Furthermore it was seen that, in neat films, the reconstructions show a higher intensity around the film edges. This is believed to be due to the relative high material contrast at the rough interfaces, as compared to the homogeneous bulk material. Much of the low frequency information within the bulk may be lost in the missing wedge.

5.2   Paper 2

The comparison of blends prepared in similar manners has been the most rewarding use of ET. E.g. the comparison of APFO-Green9:$PC_{71}BM$ (1:3) and APFO-Green9:$PC_{61}BM$ (1:3). Here ET was used in conjunction with AFM to resolve the morphology of the blends and relate that to the solar cell function. It was found that APFO-Green9:$PC_{71}BM$, being the best performing blend of the two, showed a coarser morphology, both at the surface

and in the bulk. However, the better performance of the $PC_{71}BM$ containing device is also due to the higher absorption of this fullerene derivative compared to $PC_{61}BM$.

5.3   Paper 3

The comparison of differing morphologies of otherwise identical material blends may be performed by e.g. the use of different solvents. The polymer HXS-1 was used as donor material in solar cells together with $PC_{71}BM$ in a 2:5 blend ratio. Two cell types were compared. In one the active layer was spincast from a solvent containing dichlorobenzene only, while the other type exhibited an active layer prepared from a solvent blend consisting of 2.5 % diiodooctane (DIO) and the rest dichlorobenzene. A significant morphology difference, as revealed by AFM, TEM and ET, was seen between the two types. The active layer cast with the inclusion of the high boiling point solvent DIO showed a coarser structure with larger phases than the film produced without DIO. There was also a significant difference in performance between the devices found. The coarser morphology was seen to give higher current and fill factor, with a slightly decreased open circuit voltage. Together with differing photoluminescence measurements and the small charge mobility difference, the results led to the suggestion that larger domains facilitate charge separation.

5.4   Paper 4

For TQ1:$PC_{71}BM$ (1:2) the device performance was found to depend on the spatial relation of the solar cell and spin centre during spincasting of the active layer. Solar cells further from the spin centre was seen to give higher currents than solar cells situated close to the spin centre, while the polymer photoluminescence quenching was similar. The difference in current could be correlated to a morphology difference, where the device with the coarser structure was found to give the lower current, i.e. the opposite as compared to HXS-1:$PC_{71}BM$. This points to the intricacy of charge generation in organic solar cells and the need of further studies.

5.5   Paper 5

As morphology is important for OSCs it is further analysed. Differences in preparation, e.g. stoichiometry, solvents or geometrical alterations, were studied. The results indicate a complex solar cell morphology dependence. The limited tilt angle and the low signal to noise ratio are limitations in

ET of OSCs. A way of partially remedy the problem of the missing wedge, caused by the insufficient tilt, is the use of a second, orthogonal, tilt series. Here, along with the extra data, the missing wedge is reduced to a missing pyramid. The reconstructions of OSC materials were seen to be slightly improved with this method. Decorated fibrillar structures were also studied.

5.6   Paper 6

Active layer thicknesses in OSCs are usually kept low, due to unimpressive charge mobilities. Thus, the ability to steer the light onto one or several long paths within the active layer is an attractive way of increasing light absorption and photocurrent. One way is to use a folded cell configuration and optical modelling is helpful here, to gain knowledge of the effect of parameter changes. Light absorption in folded solar cells was modelled, and combinations of different active layer thicknesses, folding angles and materials were studied. A beneficial light trapping effect was found for all studied layer thicknesses. The thinner layers were more affected by the folding, revealing a method to improve light absorption in layers adopted to low charge mobilities. In addition, the combination of two materials with differing refractive indices, forming a tandem cell, was modelled. The results showed a combined effect of light trapping and absorptance broadening.

5.7   Paper 7

The use of optically complementary materials as part of folded tandem cells is attracting. In tandem solar cells there is a need to connect subcells, often with unmatched currents or voltages. For parallel connection matching voltages is desired, while matching currents is in the case of serial connection. The folded cell has the advantage of the possibility to easily choose between types of electrical connections. In stacked planar cells, this is not always the case; cells utilising a recombination layer stacked between two active layers need balanced currents for good performance. However, from the viewpoint of minimising currents and resistive losses, serial connection may be the choice also for folded cells or planar cells with subcells separated by a spacer layer. One folded cell, with folding angle $\alpha = 20°$, was compared to four types of planar cells, with recombination or spacer layers. The maximum balanced photocurrent was compared, and showed that the folded tandem cell has the potential to deliver comparably high currents.

5.8 Paper 8

As a solar cell is supposed to be functional during the main part of the day, it also needs to cope with changing incident angles and spectra. For a single active material solar cell, the problem lies in optimising the installation angle for maximum energy output. The balancing of voltages or currents is an additional problem for tandem cells, where also the position of the subcells relative the sun is a variable parameter. Solar cells with a single active layer and tandem solar cells, in planar and folded configuration was modelled and compared. Incident light properties, i.e. angle, power and colour, during a modelled sunny summer day in mid Europe was used as input in the simulations. The expected maximum power as function of time of day and integrated over the whole day, was compared between cells. The results showed that the folded single active layer cells has the potential to deliver higher photocurrent densities during all of the day, compared to a planar cell. On the other hand, the modelling indicate that currents in folded tandem cells may be more difficult to balance as incident light properties are changing.

5.9 Paper 9

Several techniques to increase light absorption in the thin active layers of OSCs has earlier been investigated, of which one is the addition of an optical spacer between the active layer and reflecting cathode. The idea here is to alter the absorption profile in a beneficial way. We used three different active layer materials together with an optical spacer in modelled devices to calculate the maximum photocurrent dependence on active layer and spacer layer thicknesses, using two different methods. The results were similar for all materials. The optical effect of adding a spacer layer to a device with an optically optimal active layer thickness is to reduce the current. A small increase in current, when using a thinner active layer, is expected.

References

[1] Adam J. Moule. Power from plastic. *Current Opinion in Solid State & Materials Science*, 14(6):123–130, December 2010.

[2] S. Gunes, H. Neugebauer, and N. S. Sariciftci. Conjugated polymer-based organic solar cells. *Chemical Reviews*, 107(4):1324–1338, Apr 2007.

[3] H. Hoppe and N. S. Sariciftci. Organic solar cells: An overview. *Journal of Materials Research*, 19(7):1924–1945, Jul 2004.

[4] Martin A. Green, Keith Emery, Yoshihiro Hishikawa, Wilhelm Warta, and Ewan D. Dunlop. Solar cell efficiency tables (version 38). *Progress in Photovoltaics*, 19(5):565–572, August 2011.

[5] http://www.m-kagaku.co.jp/english/aboutmcc/rc/special/feature1.html.

[6] M. Jørgensen, K. Norrman, and F. C. Krebs. Stability/degradation of polymer solar cells. *Solar Energy Materials and Solar Cells*, 92(7):686–714, Jul 2008.

[7] Renee Kroon, Martijn Lenes, Jan C. Hummelen, Paul W. M. Blom, and Bert De Boer. Small bandgap polymers for organic solar cells (polymer material development in the last 5 years). *Polymer Reviews*, 48(3):531–582, 2008.

[8] J. McMurry and E. Simanek. *Fundamentals of organic chemistry*. Thomson, 6 edition, 2007.

[9] U. Gedde. *Polymer physics*. KLUWER ACADEMIC PUBL, 1999.

[10] FS Bates. Polymer-polymer phase-behavior. *Science*, 251(4996):898–905, February 1991.

[11] E Moons. Conjugated polymer blends: linking film morphology to performance of light emitting diodes and photodiodes. *Journal of Physics-Condensed Matter*, 14(47):12235–12260, December 2002.

[12] P Peumans, V Bulovic, and SR Forrest. Efficient photon harvesting at high optical intensities in ultrathin organic double-heterostructure photovoltaic diodes. *Applied Physics Letters*, 76(19):2650–2652, May 2000.

[13] M Niggemann, M Glatthaar, A Gombert, A Hinsch, and V Wittwer. Diffraction gratings and buried nano-electrodes - architectures for organic solar cells. *Thin Solid Films*, 451:619–623, March 2004.

[14] M. Niggemann, M. Glatthaar, P. Lewer, C. Muller, J. Wagner, and A. Gombert. Functional microprism substrate for organic solar cells. *Thin Solid Films*, 511:628–633, Jul 2006.

[15] K. Tvingstedt, V. Andersson, F. Zhang, and O. Inganäs. Folded reflective tandem polymer solar cell doubles efficiency. *Applied Physics Letters*, 91(12):123514, Sep 2007.

[16] S. B. Rim, S. Zhao, S. R. Scully, M. D. McGehee, and P. Peumans. An effective light trapping configuration for thin-film solar cells. *Applied Physics Letters*, 91(24):243501, Dec 2007.

[17] V. Andersson, K. Tvingstedt, and O. Inganäs. Optical modeling of a folded organic solar cell. *Journal of Applied Physics*, 103(9):094520, May 2008.

[18] R. Koeppe, N. S. Sariciftci, and A. Buchtemann. Enhancing photon harvesting in organic solar cells with luminescent concentrators. *Applied Physics Letters*, 90(18):181126, Apr 2007.

[19] G. G. Macfarlane, T. P. McLean, J. E. Quarrington, and V. Roberts. Fine structure in the absorption-edge spectrum of Si. *Phys. Rev.*, 111:1245—1254, 1958.

[20] M. Knupfer. Exciton binding energies in organic semiconductors. *Applied Physics A-Materials Science and Processing*, 77(5):623–626, Oct 2003.

[21] P. W. M. Blom, V. D. Mihailetchi, L. J. A. Koster, and D. E. Markov. Device physics of polymer : fullerene bulk heterojunction solar cells. *Advanced Materials*, 19(12):1551–1566, Jun 2007.

[22] J. K. J. van Duren, X. N. Yang, J. Loos, C. W. T. Bulle-Lieuwma, A. B. Sieval, J. C. Hummelen, and R. A. J. Janssen. Relating the morphology of poly(p-phenylene vinylene)/methanofullerene blends to solar-cell performance. *Advanced Functional Materials*, 14(5):425–434, May 2004.

[23] M. Theander, A. Yartsev, D. Zigmantas, V. Sundstrom, W. Mammo, M. R. Andersson, and O. Inganas. Photoluminescence quenching at a polythiophene/C-60 heterojunction. *Physical Review B*, 61(19):12957–12963, May 2000.

[24] D. E. Markov, E. Amsterdam, P. W. M. Blom, A. B. Sieval, and J. C. Hummelen. Accurate measurement of the exciton diffusion length in a conjugated polymer using a heterostructure with a side-chain cross-linked fullerene layer. *Journal of Physical Chemistry a*, 109(24):5266–5274, Jun 2005.

[25] P. E. Shaw, A. Ruseckas, and I. D. W. Samuel. Exciton diffusion measurements in poly(3-hexylthiophene). *Advanced Materials*, 20(18):3516–3520, Sep 2008.

[26] K. Vandewal, K. Tvingstedt, A. Gadisa, O. Inganäs, and J. V. Manca. On the origin of the open-circuit voltage of polymer-fullerene solar cells. *Nature Materials*, 8(11):904–909, Nov 2009.

[27] A. Hadipour, B. de Boer, and P. W. M. Blom. Organic tandem and multi-junction solar cells. *Advanced Functional Materials*, 18(2):169–181, Jan 2008.

[28] A. Marti and G. L. Araujo. Limiting efficiencies for photovoltaic energy conversion in multigap systems. *Solar Energy Materials and Solar Cells*, 43(2):203–222, Sep 1996.

[29] Carsten Deibel, Thomas Strobel, and Vladimir Dyakonov. Origin of the efficient polaron-pair dissociation in polymer-fullerene blends. *Physical Review Letters*, 103(3):036402, July 2009.

[30] Dirk Veldman, Oezlem Ipek, Stefan C. J. Meskers, Joergen Sweelssen, Marc M. Koetse, Sjoerd C. Veenstra, Jan M. Kroon, Svetlana S. van Bavel, Joachim Loos, and Rene A. J. Janssen. Compositional and electric field dependence of the dissociation of charge transfer excitons in alternating polyfluorene copolymer/fullerene blends. *JOURNAL OF THE AMERICAN CHEMICAL SOCIETY*, 130(24):7721–7735, JUN 18 2008.

[31] M Sprenger, S Walheim, A Budkowski, and U Steiner. Hierarchic structure formation in binary and ternary polymer blends. *Interface Science*, 11(2):225–235, April 2003.

[32] Svante Nilsson, Andrzej Bernasik, Andrzej Budkowski, and Ellen Moons. Morphology and phase segregation of spin-casted films of polyfluorene/PCBM blends. *Macromolecules*, 40(23):8291–8301, November 2007.

[33] F. L. Zhang, K. G. Jespersen, C. Björstrom, M. Svensson, M. R. Andersson, V. Sundstrom, K. Magnusson, E. Moons, A. Yartsev, and O. Inganäs. Influence of solvent mixing on the morphology and performance of solar cells based on polyfluorene copolymer/fullerene blends. *Advanced Functional Materials*, 16(5):667–674, Mar 2006.

[34] Weiwei Li, Yi Zhou, B. Viktor Andersson, L. Mattias Andersson, Yi Thomann, Clemens Veit, Kristofer Tvingstedt, Ruiping Qin, Zhishan Bo, Olle Inganäs, Uli Wuerfel, and Fengling Zhang. The effect of additive on performance and shelf-stability of HSX-1/PCBM photovoltaic devices. *Organic Electronics*, 12(9):1544–1551, September 2011.

[35] H. Hoppe, M. Niggemann, C. Winder, J. Kraut, R. Hiesgen, A. Hinsch, D. Meissner, and N. S. Sariciftci. Nanoscale morphology of conjugated polymer/fullerene-based bulk-heterojunction solar cells. *Advanced Functional Materials*, 14(10):1005–1011, Oct 2004.

[36] T. Martens, J. D'Haen, T. Munters, Z. Beelen, L. Goris, J. Manca, M. D'Olieslaeger, D. Vanderzande, L. De Schepper, and R. Andriessen. Disclosure of the nanostructure of MDMO-PPV : PCBM bulk hetero-junction organic solar cells by a combination of SPM and TEM. *Synthetic Metals*, 138(1-2):243–247, Jun 2003.

[37] M. T. Rispens, A. Meetsma, R. Rittberger, C. J. Brabec, N. S. Sariciftci, and J. C. Hummelen. Influence of the solvent on the crystal structure of PCBM and the efficiency of MDMO-PPV : PCBM 'plastic' solar cells. *Chemical Communications*, 17:2116–2118, 2003.

[38] J. Peet, J. Y. Kim, N. E. Coates, W. L. Ma, D. Moses, A. J. Heeger, and G. C. Bazan. Efficiency enhancement in low-bandgap polymer solar cells by processing with alkane dithiols. *Nature Materials*, 6(7):497–500, Jul 2007.

[39] J. K. Lee, W. L. Ma, C. J. Brabec, J. Yuen, J. S. Moon, J. Y. Kim, K. Lee, G. C. Bazan, and A. J. Heeger. Processing additives for improved efficiency from bulk heterojunction solar cells. *Journal of the American Chemical Society*, 130(11):3619–3623, Mar 2008.

[40] Yan Yao, Jianhui Hou, Zheng Xu, Gang Li, and Yang Yang. Effects of solvent mixtures on the nanoscale phase separation in polymer solar cells. *Advanced Functional Materials*, 18:1783—1789, 2008.

[41] R. P. Qin, W. W. Li, C. H. Li, C. Du, C. Veit, H. F. Schleiermacher, M. Andersson, Z. S. Bo, Z. P. Liu, O. Inganäs, U. Wuerfel, and F. L. Zhang. A planar copolymer for high efficiency polymer solar cells. *Journal of the American Chemical Society*, 131(41):14612, Oct 2009.

[42] S Walheim, M Boltau, J Mlynek, G Krausch, and U Steiner. Structure formation via polymer demixing in spin-cast films. *Macromolecules*, 30(17):4995–5003, August 1997.

[43] RAL JONES, LJ NORTON, EJ KRAMER, FS BATES, and P WILTZIUS. Surface-directed spinodal decomposition. *Physical Review Letters*, 66(10):1326–1329, March 1991.

[44] C. M. Björstrom, S. Nilsson, A. Bernasik, A. Budkowski, M. Andersson, K. O. Magnusson, and E. Moons. Vertical phase separation in spin-coated films of a low bandgap polyfluorene/pcbm blend - effects of specific substrate interaction. *Applied Surface Science*, 253(8):3906–3912, Feb 2007.

[45] CM Björstrom, A Bernasik, J Rysz, A Budkowski, S Nilsson, M Svensson, MR Andersson, KO Magnusson, and E Moons. Multilayer formation in spin-coated thin films of low-bandgap polyfluorene : PCBM blends. *Journal of Physics-Condensed Matter*, 17(50):L529–L534, DEC 21 2005.

[46] Yana Vaynzof, Dinesh Kabra, Lihong Zhao, Lay Lay Chua, Ullrich Steiner, and Richard H. Friend. Surface-directed spinodal decomposition in poly[3-hexylthiophene] and C-61-butyric acid methyl ester blends. *ACS Nano*, 5(1):329–336, January 2011.

[47] John W. Cahn. Phase separation by spinodal decomposition in isotropic systems. *The Journal of Chemical Physics*, 42(1):93–99, 1965.

[48] F. Padinger, R. S. Rittberger, and N. S. Sariciftci. Effects of postproduction treatment on plastic solar cells. *Advanced Functional Materials*, 13(1):85–88, Jan 2003.

[49] X. N. Yang, J. Loos, S. C. Veenstra, W. J. H. Verhees, M. M. Wienk, J. M. Kroon, M. A. J. Michels, and R. A. J. Janssen. Nanoscale morphology of high-performance polymer solar cells. *Nano Letters*, 5(4):579–583, Apr 2005.

[50] Y. Zhao, Z. Y. Xie, Y. Qu, Y. H. Geng, and L. X. Wang. Solvent-vapor treatment induced performance enhancement of poly(3-hexylthiophene):

methanofullerene bulk-heterojunction photovoltaic cells. *Applied Physics Letters*, 90(4):043504, Jan 2007.

[51] Christian Muller, Jonas Bergqvist, Koen Vandewal, Kristofer Tvingstedt, Ana Sofia Anselmo, Roger Magnusson, M. Isabel Alonso, Ellen Moons, Hans Arwin, Mariano Campoy-Quiles, and Olle Inganas. Phase behaviour of liquid-crystalline polymer/fullerene organic photovoltaic blends: thermal stability and miscibility. *Journal of Materials Chemistry*, 21(29):10676–10684, 2011.

[52] Xiaoniu Yang and Joachim Loos. Toward high-performance polymer solar cells: The importance of morphology control. *Macromolecules*, 40(5):1353–1362, March 2007.

[53] Lintao Hou, Ergang Wang, Jonas Bergqvist, B. Viktor Andersson, Zhongqiang Wang, Christian Muller, Mariano Campoy-Quiles, Mats R. Andersson, Fengling Zhang, and Olle Inganäs. Lateral phase separation gradients in spin-coated thin films of high-performance polymer: Fullerene photovoltaic blends. *Advanced Functional Materials*, 21(16):3169–3175, August 2011.

[54] Tiziano Agostinelli, Samuele Lilliu, John G. Labram, Mariano Campoy-Quiles, Mark Hampton, Ellis Pires, Jonathan Rawle, Oier Bikondoa, Donal D. C. Bradley, Thomas D. Anthopoulos, Jenny Nelson, and J. Emyr Macdonald. Real-time investigation of crystallization and phase-segregation dynamics in p3ht:pcbm solar cells during thermal annealing. *Advanced Functional Materials*, 21(9):1701–1708, May 2011.

[55] XN Yang, JKJ van Duren, RAJ Janssen, MAJ Michels, and J Loos. Morphology and thermal stability of the active layer in poly(p-phenylenevinylene)/methanofullerene plastic photovoltaic devices. *Macromolecules*, 37(6):2151–2158, March 2004.

[56] A. C. Mayer, Michael F. Toney, Shawn R. Scully, Jonathan Rivnay, Christoph J. Brabec, Marcus Scharber, Marcus Koppe, Martin Heeney, Iain McCulloch, and Michael D. McGehee. Bimolecular crystals of fullerenes in conjugated polymers and the implications of molecular mixing for solar cells. *Advanced Functional Materials*, 19(8):1173–1179, April 2009.

[57] CM Björstrom, KO Magnusson, and E Moons. Control of phase separation in blends of polyfluorene (co)polymers and the C-60-derivative PCBM. *Synthetic Metals*, 152(1-3):109–112, September 2005.

[58] William L. Rance, Andrew J. Ferguson, Thomas McCarthy-Ward, Martin Heeney, David S. Ginley, Dana C. Olson, Garry Rumbles, and Nikos Kopidakis. Photoinduced carrier generation and decay dynamics in intercalated and non-intercalated polymer: Fullerene bulk heterojunctions. *ACS Nano*, 5(7):5635–5646, July 2011.

[59] KG Jespersen, FL Zhang, A Gadisa, V Sundstrom, A Yartsev, and O Inganäs. Charge formation and transport in bulk-heterojunction solar cells based on alternating polyfluorene copolymers blended with fullerenes. *Organic Electronics*, 7(4):235–242, August 2006.

[60] VD Mihailetchi, LJA Koster, PWM Blom, C Melzer, B de Boer, JKJ van Duren, and RAJ Janssen. Compositional dependence of the performance of poly(p-phenylene vinylene): Methanofullerene bulk-heterojunction solar cells. *Advanced Functional Materials*, 15(5):795–801, May 2005.

[61] L. S. Roman, M. R. Andersson, T. Yohannes, and O. Inganäs. Photodiode performance and nanostructure of polythiophene/C-60 blends. *Advanced Materials*, 9(15):1164, Dec 1997.

[62] M. Dante, J. Peet, and T. Q. Nguyen. Nanoscale charge transport and internal structure of bulk heterojunction conjugated polymer/fullerene solar cells by scanning probe microscopy. *Journal of Physical Chemistry C*, 112(18):7241–7249, May 2008.

[63] Mark Dante, Andres Garcia, and Thuc-Quyen Nguyen. Three-dimensional nanoscale organization of highly efficient low band-gap conjugated polymer bulk heterojunction solar cells. *Journal of Physical Chemistry C*, 113(4):1596–1600, January 2009.

[64] O. Douheret, A. Swinnen, S. Bertho, I. Haeldermans, J. D'Haen, M. D'Olieslaeger, D. Vanderzande, and J. V. Manca. High-resolution morphological and electrical characterisation of organic bulk heterojunction solar cells by scanning probe microscopy. *Progress in Photovoltaics*, 15(8):713–726, Dec 2007.

[65] AM Belu, DJ Graham, and DG Castner. Time-of-flight secondary ion mass spectrometry: techniques and applications for the characterization of biomaterial surfaces. *Biomaterials*, 24(21):3635–3653, September 2003.

[66] M. Y. Chiu, U. S. Jeng, C. H. Su, K. S. Liang, and K. H. Wei. Simultaneous use of small- and wide-angle X-ray techniques to analyze nanometerscale phase separation in polymer heterojunction solar cells. *Advanced Materials*, 20(13):2573–2578, Jul 2008.

[67] Georg Hahner. Near edge x-ray absorption fine structure spectroscopy as a tool to probe electronic and structural properties of thin organic films and liquids. *Chemical Society Reviews*, 35(12):1244–1255, December 2006.

[68] Ana Sofia Anselmo, Lars Lindgren, Jakub Rysz, Andrzej Bernasik, Andrzej Budkowski, Mats R. Andersson, Krister Svensson, Jan van Stam, and Ellen Moons. Tuning the vertical phase separation in polyfluorene:fullerene blend films by polymer functionalization. *Chemistry of Materials*, 23(9):2295–2302, May 2011.

[69] Bofei Xue, Ben Vaughan, Chung-How Poh, Kerry B. Burke, Lars Thomsen, Andrew Stapleton, Xiaojing Zhou, Glenn W. Bryant, Warwick Belcher, and Paul C. Dastoor. Vertical stratification and interfacial structure in P3HT:PCBM organic solar cells. *Journal of Physical Chemistry C*, 114(37):15797–15805, September 2010.

[70] P. Hawkes. Electron microscope as a structure projector. In J. Frank, editor, *Electron Tomography*. Springer, 2005.

[71] C. Barry Carter David B. Williams. *Transmission Electron Microscopy.* Springer, 2009.

[72] Ludwig Reimer. *Transmission Electron Microscopy.* Springer-Verlag, 2nd edition, 1989.

[73] S. Deans. *The Radon transform and some of its applications.* Wiley, 1983.

[74] J. J. Fernandez, C. O. S. Sorzano, R. Marabini, and J. M. Carazo. Image processing and 3-D reconstruction in electron microscopy. *Ieee Signal Processing Magazine*, 23(3):84–94, May 2006.

[75] P. A. Midgley and R. E. Dunin-Borkowski. Electron tomography and holography in materials science. *Nature Materials*, 8(4):271–280, Apr 2009.

[76] M. Radermacher. Weighted back-projection methods. In J. Frank, editor, *Electron Tomography.* Springer, 2nd edition, 2005.

[77] E. V. Orlova and H. R. Saibil. Structural analysis of macromolecular assemblies by electron microscopy. *Chemical Reviews*, 2011/10/09 2011.

[78] J. Frank, T. Wagenknecht, B. F. McEwen, M. Marko, C. E. Hsieh, and C. A. Mannella. Three-dimensional imaging of biological complexity. *Journal of Structural Biology*, 138(1-2):85–91, Apr-May 2002.

[79] D. J. De Rosier and A. Klug. Reconstruction of three dimensional structures from electron micrographs. *Nature*, 217:130, 1968.

[80] R. A. Crowther, L. A. Amos, J. T Finch, D. J. De Rosier, and A Klug. Three dimensional reconstructions of spherical viruses by fourier synthesis from electron micrographs. *Nature*, 226:421, 1970.

[81] H. Jinnai, H. Hasegawa, Y. Nishikawa, G. J. A. Sevink, M. B. Braunfeld, D. A. Agard, and R. J. Spontak. 3D nanometer-scale study of coexisting bicontinuous morphologies in a block copolymer/homopolymer blend. *Macromolecular Rapid Communications*, 27(17):1424–1429, Sep 2006.

[82] H. Jinnai, Y. Shinbori, T. Kitaoka, K. Akutagawa, N. Mashita, and T. Nishi. Three-dimensional structure of a nanocomposite material consisting of two kinds of nanofillers and rubbery matrix studied by transmission electron microtomography. *Macromolecules*, 40(18):6758–6764, Sep 2007.

[83] H. Sugimori, T. Nishi, and H. Jinnai. Dual-axis electron tomography for three-dimensional observations of polymeric nanostructures. *Macromolecules*, 38(24):10226–10233, Nov 2005.

[84] K. Yamauchi, K. Takahashi, H. Hasegawa, H. Iatrou, N. Hadjichristidis, T. Kaneko, Y. Nishikawa, H. Jinnai, T. Matsui, H. Nishioka, M. Shimizu, and H. Fukukawa. Microdomain morphology in an ABC 3-miktoarm star terpolymer: A study by energy-filtering TEM and 3D electron tomography. *Macromolecules*, 36(19):6962–6966, Sep 2003.

[85] Y. Ikeda, A. Katoh, J. Shimanuki, and S. Kohjiya. Nano-structural observation of in situ silica in natural rubber matrix by three dimensional transmission electron microscopy. *Macromolecular Rapid Communications*, 25(12):1186–1190, Jun 2004.

[86] R. J. SPONTAK, M. C. WILLIAMS, and D. A. AGARD. 3-dimensional study of cylindrical morphology in an SBS block copolymer. *Journal of Electron Microscopy Technique*, 7(2):143–143, Oct 1987.

[87] B. V. Andersson, A. Herland, S. Masich, and O. Inganäs. Imaging of the 3D nanostructure of a polymer solar cell by electron tomography. *Nano Letters*, 9(2):853–855, Feb 2009.

[88] S. Barrau, V. Andersson, F. L. Zhang, S. Masich, J. Bijleveld, M. R. Andersson, and O. Inganäs. Nanomorphology of bulk heterojunction organic solar cells in 2D and 3D correlated to photovoltaic performance. *Macromolecules*, 42(13):4646–4650, Jul 2009.

[89] S. S. van Bavel, E. Sourty, G. de With, and J. Loos. Three-dimensional nanoscale organization of bulk heterojunction polymer solar cells. *Nano Letters*, 9(2):507–513, Feb 2009.

[90] Svetlana van Bavel, Erwan Sourty, Gijsbertus de With, Kai Frolic, and Joachim Loos. Relation between photoactive layer thickness, 3D morphology, and device performance in P3HT/PCBM bulk-heterojunction solar cells. *Macromolecules*, 42(19):7396–7403, October 2009.

[91] Svetlana van Bavel, Erwan Sourty, Gijsbertus de With, Sjoerd Veenstra, and Joachim Loos. Three-dimensional nanoscale organization of polymer solar cells. *Journal of Materials Chemistry*, 19(30):5388–5393, 2009.

[92] S. D. Oosterhout, M. M. Wienk, S. S. van Bavel, R. Thiedmann, L. J. A. Koster, J. Gilot, J. Loos, V. Schmidt, and R. A. J. Janssen. The effect of three-dimensional morphology on the efficiency of hybrid polymer solar cells. *Nature Materials*, 8(10):818–824, Oct 2009.

[93] James C. Hindson, Zineb Saghi, Juan-Carlos Hernandez-Garrido, Paul A. Midgley, and Neil C. Greenham. Morphological study of nanoparticle-polymer solar cells using high-angle annular dark-field electron tomography. *Nano Letters*, 11(2):904–909, February 2011.

[94] Andrew A. Herzing, Lee J. Richter, and Ian M. Anderson. 3D nanoscale characterization of thin-film organic photovoltaic device structures via spectroscopic contrast in the TEM. *Journal of Physical Chemistry C*, 114(41):17501–17508, October 2010.

[95] Svetlana S. van Bavel and Joachim Loos. Volume organization of polymer and hybrid solar cells as revealed by electron tomography. *Advanced Functional Materials*, 20(19):3217–3234, October 2010.

[96] Svetlana van Bavel, Sjoerd Veenstra, and Joachim Loos. On the importance of morphology control in polymer solar cells. *Macromolecular Rapid Communications*, 31(21):1835–1845, November 2010.

[97] Stefan D. Oosterhout, L. Jan Anton Koster, Svetlana S. van Bavel, Joachim Loos, Ole Stenzel, Ralf Thiedmann, Volker Schmidt, Bert Campo, Thomas J. Cleij, Laurence Lutzen, Dirk Vanderzande, Martijn M. Wienk, and Rene A. J. Janssen. Controlling the morphology and efficiency of hybrid zno:polythiophene solar cells via side chain functionalization. *Advanced Energy Materials*, 1(1):90–96, January 2011.

[98] R. A. Crowther, D. J. De Rosier, and A. Klug. The reconstruction of a three-dimensional structure from projections and its application to electron microscopy. *Proc. Roy. Soc. London a*, 317:319–340, 1970.

[99] J. Loos, E. Sourty, K. Lu, B. Freitag, D. Tang, and D. Wall. Electron tomography on micrometer-thick specimens with nanometer resolution. *Nano Letters*, 9(4):1704–1708, April 2009.

[100] PA Midgley, M Weyland, JM Thomas, and BFG Johnson. Z-contrast tomography: a technique in three-dimensional nanostructural analysis based on rutherford scattering. *Chemical Communications*, (10):907–908, 2001.

[101] G Cardone, K Grunewald, and AC Steven. A resolution criterion for electron tomography based on cross-validation. *Journal of Structural Biology*, 151(2):117–129, August 2005.

[102] M van Heel and M Schatz. Fourier shell correlation threshold criteria. *Journal of Structural Biology*, 151(3):250–262, September 2005.

[103] Ergang Wang, Lintao Hou, Zhongqiang Wang, Stefan Hellstrom, Fengling Zhang, Olle Inganäs, and Mats R. Andersson. An easily synthesized blue polymer for high-performance polymer solar cells. *Advanced Materials*, 22(46):5240–5244, December 2010.

[104] P PENCZEK, M MARKO, K BUTTLE, and J FRANK. Double-tilt electron tomography. *Ultramicroscopy*, 60(3):393–410, October 1995.

[105] I. Arslan, J. R. Tong, and P. A. Midgley. Reducing the missing wedge: High-resolution dual axis tomography of inorganic materials. *Ultramicroscopy*, 106(11-12):994–1000, Oct-Nov 2006.

[106] B. Vestergaard, M. Groenning, M. Roessle, J. S. Kastrup, M. van de Weert, J. M. Flink, S. Frokjaer, M. Gajhede, and D. I. Svergun. A helical structural nucleus is the primary elongating unit of insulin amyloid fibrils. *Plos Biology*, 5(5):1089–1097, May 2007.

[107] C Kubel, A Voigt, R Schoenmakers, M Otten, D Su, TC Lee, A Carlsson, and J Bradley. Recent advances in electron tomography: TEM and HAADF-STEM tomography for materials science and semiconductor applications. *Microscopy and Microanalysis*, 11(5):378–400, October 2005.

[108] AH Janssen, CM Yang, Y Wang, F Schuth, AJ Koster, and KP de Jong. Localization of small metal (oxide) particles in SBA-15 using bright-field electron tomography. *Journal of Physical Chemistry B*, 107(38):10552–10556, September 2003.

[109] AJ Koster, U Ziese, AJ Verkleij, AH Janssen, and KP de Jong. Three-dimensional transmission electron microscopy: A novel imaging and characterization technique with nanometer scale resolution for materials science. *Journal of Physical Chemistry B*, 104(40):9368–9370, October 2000.

[110] LAA Pettersson, LS Roman, and O Inganäs. Modeling photocurrent action spectra of photovoltaic devices based on organic thin films. *Journal of Applied Physics*, 86(1):487–496, July 1999.

[111] NK Persson, H Arwin, and O Inganäs. Optical optimization of polyfluorene-fullerene blend photodiodes. *Journal of Applied Physics*, 97(3):034503, February 2005.

[112] E Centurioni. Generalized matrix method for calculation of internal light energy flux in mixed coherent and incoherent multilayers. *Applied Optics*, 44(35):7532–7539, December 2005.

[113] NK Persson, M Schubert, and O Inganäs. Optical modelling of a layered photovoltaic device with a polyfluorene derivative/fullerene as the active layer. *Solar Energy Materials and Solar Cells*, 83(2-3):169–186, June 2004.

[114] U Zhokhavets, G Gobsch, H Hoppe, and NS Sariciftci. A systematic study of the anisotropic optical properties of thin poly(3-octylthiophene)-films in dependence on growth parameters. *Thin Solid Films*, 451:69–73, March 2004.

[115] U Zhokhavets, R Goldhahn, G Gobsch, M Al-Ibrahim, HK Roth, S Sensfuss, E Klemm, and DAM Egbe. Anisotropic optical properties of conjugated polymer and polymer/fullerene films. *Thin Solid Films*, 444(1-2):215–220, November 2003.

[116] Nils-Krister Persson and Olle Inganäs. Organic tandem solar cells - modelling and predictions. *Solar Energy Materials and Solar Cells*, 90(20):3491–3507, December 2006.

[117] B. Viktor Andersson, Nils-Krister Persson, and Olle Inganas. Comparative study of organic thin film tandem solar cells in alternative geometries. *Journal of Applied Physics*, 104(12):124508, December 2008.

[118] J. Y. Kim, K. Lee, N. E. Coates, D. Moses, T. Q. Nguyen, M. Dante, and A. J. Heeger. Efficient tandem polymer solar cells fabricated by all-solution processing. *Science*, 317(5835):222–225, Jul 2007.

[119] Gilles Dennler, Karen Forberich, Tayebeh Ameri, Christoph Waldauf, Patrick Denk, Christoph J. Brabec, Kurt Hingerl, and Alan J. Heeger. Design of efficient organic tandem cells: On the interplay between molecular absorption and layer sequence. *Journal of Applied Physics*, 102(12):123109, December 2007.

[120] LS Roman, O Inganäs, T Granlund, T Nyberg, M Svensson, MR Andersson, and JC Hummelen. Trapping light in polymer photodiodes with soft embossed gratings. *Advanced Materials*, 12(3):189–195, February 2000.

[121] Kristofer Tvingstedt, Nils-Krister Persson, Olle Inganäs, Aliaksandr Rahachou, and Igor V. Zozoulenko. Surface plasmon increase absorption in polymer photovoltaic cells. *Applied Physics Letters*, 91(11):113514, September 2007.

[122] Harry A. Atwater and Albert Polman. Plasmonics for improved photovoltaic devices. *Nature Materials*, 9(3):205–213, March 2010.

[123] Kristofer Tvingstedt, Simone Dal Zilio, Olle Inganäs, and Massimo Tormen. Trapping light with micro lenses in thin film organic photovoltaic cells. *Optics Express*, 16(26):21608–21615, December 2008.

[124] Yinhua Zhou, Fengling Zhang, Kristofer Tvingstedt, Wenjing Tian, and Olle Inganäs. Multifolded polymer solar cells on flexible substrates. *Applied Physics Letters*, 93(3):033302, July 2008.

[125] D. W. Zhao, X. W. Sun, C. Y. Jiang, A. K. K. Kyaw, G. Q. Lo, and D. L. Kwong. Efficient tandem organic solar cells with an Al/MoO3 intermediate layer. *Applied Physics Letters*, 93(8):083305, August 2008.

[126] Gilles Dennler, Hans-Jurgen Prall, Robert Koeppe, Martin Egginger, Robert Autengruber, and Niyazi Serdar Sariciftci. Enhanced spectral coverage in tandem organic solar cells. *Applied Physics Letters*, 89(7):073502, August 2006.

[127] A Yakimov and SR Forrest. High photovoltage multiple-heterojunction organic solar cells incorporating interfacial metallic nanoclusters. *Applied Physics Letters*, 80(9):1667–1669, March 2002.

[128] Jan Gilot, Martijn M. Wienk, and Rene A. J. Janssen. Double and triple junction polymer solar cells processed from solution. *Applied Physics Letters*, 90(14):143512, April 2007.

[129] Afshin Hadipour, Bert de Boer, Jurjen Wildeman, Floris B. Kooistra, Jan C. Hummelen, Mathieu G. R. Turbiez, Martijn M. Wienk, Rene A. J. Janssen, and Paul W. M. Blom. Solution-processed organic tandem solar cells. *Advanced Functional Materials*, 16(14):1897–1903, September 2006.

[130] A. Meyer and H. Ade. The effect of angle of incidence on the optical field distribution within thin film organic solar cells. *Journal of Applied Physics*, 106(11):113101, December 2009.

[131] W. Strauss. *Partial differential equations. An introduction*. Wiley, 1992.

[132] J. Jin. *The finite element method in electromagnetics*. Wiley, 2002.

[133] B. Viktor Andersson, Uli Wuerfel, and Olle Inganäs. Full day modelling of V-shaped organic solar cell. *Solar Energy*, 85(6):1257–1263, June 2011.

[134] JY Kim, SH Kim, HH Lee, K Lee, WL Ma, X Gong, and AJ Heeger. New architecture for high-efficiency polymer photovoltaic cells using solution-based titanium oxide as an optical spacer. *Advanced Materials*, 18(5):572–576, March 2006.

[135] Jae Kwan Lee, Nelson E. Coates, Shinuk Cho, Nam Sung Cho, Daniel Moses, Guillermo C. Bazan, Kwanghee Lee, and Alan J. Heeger. Efficacy of TiOx optical spacer in bulk-heterojunction solar cells processed with 1,8-octanedithiol. *Applied Physics Letters*, 92(24):243308, June 2008.

[136] Jan Gilot, Ionut Barbu, Martijn M. Wienk, and Rene A. J. Janssen. The use of zno as optical spacer in polymer solar cells: Theoretical and experimental study. *Applied Physics Letters*, 91(11):113520, September 2007.

[137] B. Viktor Andersson, David M. Huang, Adam J. Moule, and Olle Inganäs. An optical spacer is no panacea for light collection in organic solar cells. *Applied Physics Letters*, 94(4):043302, January 2009.